ORP5 TRANSFERS PHOSPHATIDYLSERINE TO MITOCHONDRIA AND REGULATES MITOCHONDRIAL CALCIUM UPTAKE AT ENDOPLASMIC RETICULUM - MITOCHONDRIA CONTACT SITES

Leila Rochin[1], Cécile Sauvanet[1]*, Eeva Jääskeläinen[2]*, Audrey Houcine[3]*, Amita Arora[2], Annukka M. Kivelä[2], Xingjie MA[5,10], Eyra Marien[4], Jonas Dehairs[4], Romain Le Bars[6], Julie Neveu[1], Elena Santonico[7], Johannes V. Swinnen[4], David Bernard[5], David Tareste[8], Vesa M. Olkkonen[2,9], and Francesca Giordano[1#]

[1] Institute for Integrative Biology of the Cell (I2BC), CEA, CNRS, Univ. Paris-Sud, Université Paris-Saclay, Gif-sur-Yvette cedex 91198, France.

[2] Minerva Foundation Institute for Medical Research, Biomedicum 2U, FI-00290 Helsinki, Finland

[3] Institut Jacques Monod, CNRS, UMR7592, Université Paris Diderot, Sorbonne Paris Cité, F-75013 Paris, France

[4] Laboratory of Lipid Metabolism and Cancer, Department of Oncology, KU Leuven, Leuven B-3000, Belgium.

[5] Centre de Recherche en Cancérologie de Lyon, UMR INSERM U1052/CNRS 5286, Centre Léon Bérard, 69373 LYON Cedex 08, France

[6] Imagerie-Gif, Light Microscopy Facility, Institute for Integrative Biology of the Cell (I2BC), CEA, CNRS, Univ. Paris-Sud, Université Paris-Saclay, Gif-sur-Yvette cedex 91198, France

[7] University of Rome Tor Vergata, via della ricerca scientifica, dipartimento di Biologia, 00133, Italy

[8] Institute of Psychiatry and Neuroscience of Paris (IPNP), UMR-S1266 INSERM-Paris Descartes University, Paris, France

[9] Department of Anatomy, Faculty of Medicine, FI-00014 University of Helsinki, Finland

[10] Xingjie MA present address: The Affiliated Hospital of Yangzhou University, Yangzhou University, Yangzhou, China

* These authors contributed equally to this work

Correspondence to: francesca.giordano@i2bc.paris-saclay.fr

SUMMARY

Mitochondria are dynamic organelles essential for cell survival whose structural and functional integrity rely on selective and regulated transport of lipids from/to the endoplasmic reticulum (ER) and across the two mitochondrial membranes. As they are not connected by vesicular transport, the exchange of lipids between ER and mitochondria occurs at sites of close organelle apposition called membrane contact sites. However, the mechanisms and proteins involved in these processes are only beginning to emerge. Here, we show that ORP5/8 mediate non-vesicular transport of Phosphatidylserine (PS) from the ER to mitochondria in mammalian cells. We also show that ER-mitochondria contacts where ORP5/8 reside are physically and functionally linked to the MIB/MICOS complexes that bridge the mitochondrial membranes, cooperating with them to facilitate PS transfer from the ER to the mitochondria. Finally, we show that ORP5 but not ORP8, additionally regulates import of calcium to mitochondria and consequently cell senescence.

KEYWORDS

Membrane contact sites, mitochondria, ORP, lipid transfer, calcium

INTRODUCTION

Vesicular trafficking is the major pathway for transport of proteins and metabolites, such as lipids, between membranes. However, an alternative route, which is vesicle-independent, occurs at regions of close inter-organelle membrane proximity (within less than 30 nm) also called membrane contact sites (Scorrano, De Matteis et al., 2019). This route is particularly important to preserve membrane composition, integrity and identity of the intracellular organelles such as the mitochondria that are largely excluded from the classical vesicle-mediated trafficking pathways. Like other organelles, mitochondria can be closely associated with the endoplasmic reticulum (ER), the major site of lipid synthesis and the major intracellular calcium (Ca^{2+}) store. ER membrane subdomains closely apposed to the mitochondria are called mitochondria-associated ER membranes (MAMs) and they facilitate the exchange of Ca^{2+} and lipids between the two organelles (Herrera-Cruz & Simmen, 2017, Tatsuta, Scharwey et al., 2014, Vance, 2014)

Mitochondria are involved in a plethora of cellular processes including energy production, lipid metabolism, Ca^{2+} homeostasis and apoptosis. To fulfill their numerous functions, mitochondria need to maintain a defined membrane composition by receiving essential lipids and lipid precursors from the ER through membrane contact sites (Giordano, 2018, Vance & Tasseva, 2013).

Increasing lines of evidence suggest that lipid transfer proteins (LTPs) play a major role in regulating the lipid composition of membranous organelles by facilitating non-

75 vesicular lipid transport at membrane contact sites. In recent years, several tethering
76 complexes with lipid transfer activity have been identified at membrane contact sites
77 between the ER and other intracellular organelles including the plasma membrane (PM)
78 in yeast as well as in mammalian cells. However, our knowledge of how lipids are
79 exchanged at ER-mitochondria membrane contact sites remains still rudimentary, and
80 the LTPs that localize and function at these sites are largely unknown. The best-studied
81 lipid transfer/tethering complex at ER-mitochondria contact sites is the yeast ER-
82 mitochondria encounter structure (ERMES) (Kornmann et al 2009, Lang et al 2015) that
83 bridges the ER and the mitochondrial membranes and also facilitates the exchange
84 of phospholipids (in particular phosphatidylcholine, PC) between them. In metazoans,
85 very little is known on how lipids are exchanged at ER-mitochondria membrane
86 contact sites and about the proteins involved in this process. Some tethers at
87 mammalian ER-mitochondria contact sites have started to emerge in the past years
88 (Gatta and Levine 2017), including the Mitochondrial Ca^{2+} Uniporter (MCU)–Voltage
89 Dependent Anion Channel (VDAC)–Glucose Regulated Protein 75 (GRP75)–Inositol
90 Triphosphate Receptor (IP3R) machinery involved in Ca^{2+} import from the ER to
91 mitochondria (Rizzuto et al. 2009), the Protein tyrosine phosphatase interacting
92 protein 51 (PTPIP51)–Vesicle-associated membrane protein-associated protein B
93 (VAPB) complex (Stoica et al 2014) alteration of which induces defects in ER-
94 mitochondria tethering and Ca^{2+} exchanges, and Pdzd8, a recently identified
95 tethering protein and proposed paralog of the ERMES subunit Mmm1, also required
96 for the regulation of ER-mitochondria contacts and mitochondrial Ca^{2+} uptake
97 (Hirabayashi, Kwon et al., 2017). However, none of these proteins has been directly
98 involved in non-vesicular lipid transport between ER and mitochondrial membranes.
99 Lately, a mammalian LTP, VPS13A, has been shown to localize at membrane

100 contact sites including those between ER and mitochondria, but its function in lipid
101 transport at these sites has not been elucidated yet (Kumar, Leonzino et al., 2018).
102 The Oxysterol binding protein (OSBP)-related proteins constitute a large family of
103 LTPs conserved from yeast (Osh) to humans (ORP) and localized to different
104 subcellular sites, shown in several cases to be membrane contact sites. A common
105 feature of all ORPs is the presence of an OSBP-related lipid-binding/transfer (ORD)
106 domain. Most ORP proteins contain a two phenylalanines (FF) in an acidic tract
107 (FFAT)-motif that binds ER-localized VAP proteins and a pleckstrin homology (PH)
108 domain that interacts with lipids or proteins in distinct non-ER organelle membranes.
109 Two members of this family, ORP5 and ORP8, do not contain an FFAT motif but are
110 directly anchored to the ER through a C-terminal trans-membrane segment. We have
111 recently shown that ORP5 and ORP8 localize to ER-mitochondria contact sites
112 where they play a key role in maintaining mitochondrial morphology and respiratory
113 function (Galmes et al. 2016). ORP5 and ORP8 have been previously shown to
114 transfer phosphatidylserine (PS) from the cortical ER to the PM, in counter-exchange
115 with the phosphoinositides Phosphatidylinositol-4-phosphate (PI4P) and
116 Phosphatidylinositol 4,5-bisphosphate (PIP_2) (Chung et al. 2015; Ghai et al, 2017).
117 Interestingly, transport of PS occurs also at ER-mitochondria contact sites. Newly
118 synthesized PS, by the ER-localized PS-Synthase 1 (PSS1), is shuttled from the ER to
119 the outer mitochondrial membrane (OMM) and from OMM to inner mitochondrial
120 membrane (IMM) where it is rapidly converted to phosphatidylethanolamine (PE) by the
121 PS-decarboxylase enzyme PISD (Vance, 1990, Vance & Tasseva, 2013). At the IMM,
122 PE plays crucial roles in maintaining mitochondrial tubular morphology and therefore in
123 mitochondrial respiratory functions (Joshi, Thompson et al., 2012, Steenbergen,
124 Nanowski et al., 2005). Regardless of extensive studies on PS transport between ER

125 and mitochondria since its first discovery more than 20 years ago (Vance, 1990), the
126 underlying mechanisms and proteins involved are still elusive.

127 Membrane contact sites exist also between the OMM and the IMM and are
128 mediated by the Mitochondrial Intermembrane space Bridging (MIB) and Mitochondrial
129 Contact sites and Cristae junction Organizing System (MICOS) complexes. The MICOS
130 complex (composed of seven proteins: Mitofilin, CHCHD3, CHCHD6, APOO, QIL1,
131 APOOL and MINOS1) is preferentially located at Cristae Junctions (CJ), tubular
132 structures that connect the IMM to the cristae, and it is necessary for CJ formation,
133 cristae morphology and mitochondria function (Harner, Korner et al., 2011, Huynen,
134 Muhlmeister et al., 2016, Ott, Dorsch et al., 2015, Wollweber, von der Malsburg et al.,
135 2017). The integral IMM protein Mitofilin is the central component of the MICOS
136 complex and carries a large domain exposed to the mitochondria intermembrane
137 space (IMS) that interacts with the OMM Sorting and Assembly Machinery (SAM) to
138 form the MIB complex (Friedman, Mourier et al., 2015, Guarani, McNeill et al., 2015).
139 The SAM complex is constituted of SAM50 (a pore-forming β-barrel protein),
140 Metaxin1 and 2, and is involved in the membrane insertion and assembly of
141 mitochondrial β-barrel proteins, such as VDAC (Hohr, Lindau et al., 2018, Kozjak,
142 Wiedemann et al., 2003, Kozjak-Pavlovic, Ross et al., 2007) (see cartoon in Figure
143 10). However, whether and how OMM-IMM contact sites are linked to ER-
144 mitochondria contacts in mammalian cells is still largely unknown.

145 Here we show that ORP5 and ORP8 are the LTPs that transfer PS from the ER
146 to the mitochondria at ER-mitochondria contact sites in mammalian cells. We also
147 show that ORP5/8 are physically and functionally connected with Sorting Assembly
148 Machinery 50 (SAM50) and Mitofilin with which they cooperate to facilitate PS
149 transport from the ER to the mitochondrial membranes and consequently the

150 synthesis of mitochondrial PE. Finally, we uncover an additional role for ORP5, but not
151 ORP8, in regulating Ca^{2+} import to mitochondria, through regulation of SAM50-VDAC
152 protein levels. Our findings reveal a novel link between lipid and Ca^{2+} transport at ER-
153 mitochondria contact sites and provide mechanistic insight to the specific role of
154 ORP5 in modulating cellular senescence.
155

156 **RESULTS**

157 **ORP5 and ORP8 transport PS from the ER to the mitochondria at ER-**
158 **mitochondria contact sites**

159 We have recently reported that ORP5 and ORP8, shown to transfer lipids at ER-PM
160 contacts, localize also to ER-mitochondria contact sites (Galmes, Houcine et al., 2016).
161 However, their role in lipid transport at ER-mitochondria contacts still remains to be
162 established. Taking into account their role in counter-exchanging PS with the PM
163 phosphoinositides PI4P and PIP_2 at ER-PM contacts (Chung et al. 2015; Ghai et al,
164 2017), we hypothesized that ORP5 and ORP8 could also mediate PS transport at ER-
165 mitochondria contact sites.
166 The ORD domain of ORP8 has been shown to transfer PS (in counter-transport with
167 PI4P or PIP_2) between liposome membranes *in vitro* (Chung et al. 2015; Ghai et al,
168 2017). Since PI4P and PIP_2 are not present in mitochondrial membranes it is possible
169 that at ER-mitochondria contact sites ORP5/8 might transport other phospholipids,
170 such as PE, back to the ER. However, no study so far has ever addressed the ability
171 of ORP5 and ORP8 ORD domains (ORD5, ORD8) to transfer other phospholipids
172 between liposomes *in vitro.* First, to compare and study the role of ORD5 and ORD8
173 in the transfer of phospholipids *in vitro*, we purified the recombinant ORD5 (aa 265-
174 703) and ORD8 (aa 328-767) in bacteria (Escherichia coli) (Fig. S1a) and analyzed

175 their lipid transfer ability by measuring the transport of fluorescent phospholipids
176 (TopFluor-PS, -PC or -PE) from donor to acceptor liposomes *in vitro*. Donor
177 liposomes containing fluorescent phospholipids and biotinylated lipids (liposomes
178 composed of 1 mol% TopFluor-PS, -PC or -PE, 2 mol% of biotinylated-PE, and 97
179 mol% POPC) were first immobilized on streptavidin beads and then mixed with
180 acceptor liposomes (composed of 100 mol % POPC) in the presence or absence of
181 ORP5/8 ORD domains (Fig. 1a). After 1 hour at 37°C, acceptor liposomes were
182 recovered from the supernatant and their fluorescence was measured (Fig. 1a). Our
183 results show that both ORD5 and ORD8 transfer PS, but not PC and PE, from donor
184 to acceptor liposomes (Fig. 1b). They also reveal that ORD5 and ORD8 share
185 equivalent abilities to transfer PS *in vitro*. To confirm that fluorescent lipids were
186 indeed transferred to the acceptor liposomes, a fraction of the reaction supernatant
187 was floated on a Nycodenz density gradient by ultracentrifugation and the
188 fluorescence in the top fraction of the gradient (containing floated acceptor
189 liposomes) was measured (Figure S1b). Fluorescence of TopFluor-PS in the
190 acceptor liposomes was maintained after their floatation, confirming its effective
191 transfer between liposomes *in vitro*.

192 Next, we addressed whether ORP5 and ORP8 could mediate non-vesicular
193 transfer of PS at ER-mitochondria contact sites *in situ*. As the ER-derived PS is the
194 major precursor for mitochondrial PE, if ORP5 and ORP8 mediate non-vesicular
195 transport of PS from the ER to the mitochondria, then their absence should lead to a
196 reduction of mitochondrial PE. To test this, we used Percoll gradient-based
197 subcellular fractionation (Galmes et al. 2016) to isolate pure mitochondria from HeLa
198 cells where ORP5 or ORP8 were transiently silenced by RNAi. We chose to use a
199 transient knockdown as it overcomes the limits and/or compensatory effects on lipid

200 transport/biosynthetic pathways that other stable approaches could induce. The
201 purity of mitochondria and of the other subcellular fractions was verified in control,
202 ORP5 and ORP8 knockdown conditions by western blotting (WB) (Fig. 1c). As
203 controls for the purity of subcellular fractions, the samples were probed for
204 cytochrome c as mitochondrial marker and IP3R-3 as a MAM-enriched marker. All
205 markers were highly enriched in their respective fractions and were absent in the
206 others. In accord with our previous study (Galmes et al., 2016), ORP5 and ORP8
207 were enriched in the MAM fraction and absent in the mitochondria fraction of control
208 cells. On the contrary, they were strongly suppressed in ORP5 and ORP8
209 knockdown cell lysates and in the respective MAM fractions (Fig. 1c). The PE content
210 of purified mitochondria from ORP5 and ORP8 knockdown was then analyzed by
211 mass spectrometry (MS)-based lipidomics, revealing a reduction of PE levels in
212 mitochondria isolated from ORP5 and ORP8 knockdown cells of 34% and 20%,
213 respectively, as compared to control cells (Fig. 1d). Interestingly, PE levels of the
214 total cells were unchanged, indicating a specific effect of ORP5 or ORP8 depletion
215 on mitochondrial PE.

216 In subsequent experiments, we measured the levels of mitochondrial PE newly
217 synthesized from the ER-derived PS by using a radiometric PS-to-PE conversion
218 assay *in situ* (Shiao, Lupo et al., 1995) in silenced or control HeLa cells (Fig. 1e).
219 This assay allows the monitoring of PS transfer from the ER to mitochondria by
220 measuring the levels of radioactive PS and PS-derived PE by thin layer
221 chromatography (TLC) after 18h of incorporation of radioactive L-[^{3}H(G)]-serine into
222 the cells. A significant decrease in the levels of newly synthetized PE was found in
223 ORP5 knockdown and in ORP5+ORP8 double-knockdown cells (Fig. 1e). The
224 decrease was stronger in ORP5+ORP8 double-knockdown cells, indicating a

225 cooperative effect of ORP5 and ORP8 in this process. A slight decrease was also
226 found in ORP8 knockdown cells, although not statistically significant, suggesting a
227 major role of ORP5 compared to ORP8 in PS transfer at ER-mitochondria contact
228 sites *in situ*. As [^{3}H]-serine radioactivity could be incorporated to PE also via an
229 alternative pathway involving sphingosine (Hanada, Nishijima et al., 1992), we next
230 sought to address the contribution of this pathway to PE labeling, by repeating the
231 experiments in control and ORP5 knockdown cells in the presence of β-chloro-L-
232 alanine, an inhibitor of serine palmitoyltransferase (Chen, Born et al., 1993). The PS-
233 to-PE conversion was not significantly affected in both control (~3% of reduction) and
234 ORP5 knockdown cells (~9% of reduction). On the contrary, PS-to-PE conversion
235 was significantly reduced in treated and untreated ORP5 knockdown cells (~17% and
236 ~23% respectively), as compared to control (Fig. 1f). These data show that more
237 than 90% of serine labeling occurs via PS in HeLa cells, that is in accord with a
238 previous work in another cell type, the BHK cells, showing that only a minor PE
239 species are labeled from the sphingosine-PE pathway (Heikinheimo & Somerharju,
240 1998). Lastly, the decrease in PE could be simply due to a decrease in the protein
241 levels of PS-decarboxylase (PISD) or in the PS-Synthase 1 (PSS1) enzymes
242 mediating PS-to-PE conversion on mitochondria or PS synthesis in the ER,
243 respectively. To exclude this possibility we analyzed the protein levels of PISD and
244 PSS1 enzymes by WB in ORP5, ORP8, ORP5+ORP8 knockdown cells and
245 compared them to control cells (Fig. 1g). We found no significant difference but
246 rather a slight increase in upon ORP5 and/or ORP8 knockdowns. Overall these data
247 confirm that the reduction in mitochondrial PE induced by depletion of ORP5 is
248 essentially due to the decrease in PS transfer from the ER to the mitochondria (Fig.
249 1h).

ORP5 and ORP8 knockdown affect mitochondria morphology and respiratory function but not the abundance of ER-mitochondria contact sites

Even a modest reduction (22-27%) of mitochondrial PE levels in mammalian cells have been shown to profoundly alter the morphology of mitochondrial cristae as well as mitochondria functions (Tasseva, Bai et al., 2013). Thus, the decrease in mitochondrial PE in ORP5 and ORP8 knockdowns is in accord with our previous electron microscopy (EM) observations that knockdown of ORP5 or ORP8 alters the architecture of the cristae, while ER-mitochondria contact sites with normal morphology were still visible (Galmes et al., 2016). However, our previous study did not rule out that these contact sites could be affected in their number/size. To test whether the effects on PS transport at ER-mitochondria contacts were specific of ORP5 and ORP8 loss of function or simply due to a decrease of ER-mitochondria contacts induced by their knockdown, we quantified the abundance of ER-mitochondria contact sites by EM in control and ORP5, ORP8, ORP5+ORP8 knockdown cells. To facilitate the visualization of the ER we transfected the cells with a HRP-KDEL construct (carrying a horseradish peroxidase (HRP) tagged with an ER retention motif) that stains the ER with a dark signal. Our quantifications revealed that ORP5, ORP8 or ORP5+ORP8 knockdowns did not affect the extent of ER-mitochondria contact sites (Fig. 2a-2b). These results indicate that ORP5 and ORP8 act exclusively as LTPs and not as tethers (Fig. 1h). Additionally, 52% of mitochondria in ORP5+ORP8 double-knockdown cells display aberrant cristae morphology versus 9% in control cells (Fig. 2a-2c). These defects in cristae morphology were similar to those previously shown in the case of ORP5 and ORP8 individual knockdowns (Galmes et al., 2016). However, the % of mitochondria with altered morphology in ORP5+ORP8 double-knockdown cells was higher as

276 compared to ORP8 knockdown (Galmes et al., 2016), possibly reflecting the stronger
277 effect of ORP5+ORP8 double-knockdown on PS transport at ER-mitochondria
278 contact sites. We had previously shown that ORP5 knockdown induced a reduction
279 in the basal mitochondrial oxygen consumption rate (OCR_{BAS}), indicative of reduced
280 mitochondria respiratory activity (Galmes et al., 2016). However, it remained still
281 questioned whether ORP8 could partially compensate the reduced OCR_{BAS} and/or if
282 this reduction could be exacerbated under metabolic stress conditions. Thus, we
283 monitored mitochondria OCR in control, in ORP5 and in ORP5+ORP8 double-
284 knockdown cells in basal and in stress conditions (Fig. 2d). ORP5 knockdown induced a
285 significant reduction in both OCR_{BAS} (~37%) and OCR upon FCCP treatment (OCR_{FCCP}) (~36%).
286 Interestingly, the decrease in in OCR_{BAS} and OCR_{FCCP} measured upon ORP5+ORP8
287 double-knockdown was quite similar to the decrease in ORP5 knockdown. These
288 data uncover a major role of ORP5 in preserving mitochondrial respiratory activity, in
289 accord with its major role in PS transfer at ER-mitochondria contact sites.
290

291 **ER-mitochondria contact sites marked by ORP5/8 are physically connected to**
292 **mitochondrial membranes via ORP5/8 interaction with the mitochondrial**
293 **intermembrane space bridging (MIB) complex**

294 To investigate whether ORP5/8 localize to specific ER-mitochondria contact site
295 subdomains we performed a morphological analysis of ORP5 localization by
296 immuno-EM (IEM) on ultrathin cryosections from HeLa cells transfected with HA-
297 ORP5 or EGFP-ORP5. The advantage of analyzing ORP5 localization is its
298 preferential localization to contact sites as compared to ORP8 (Galmes et al. 2016),
299 which remains also largely present within the reticular ER. Interestingly, the majority
300 of ORP5 gold particles was found to localize to ER elements in a very close proximity

301 (86% within 0-100 nm distances, 50% of which within 50 nm) to the CJ (arrow, Fig.
302 2a-b), tubular structures that connect the IMM to the cristae. To exclude that ORP5
303 localization near CJ is not a consequence of its distribution throughout the ER
304 membranes, we sought to determine if other ER proteins have a similar frequency of
305 proximity to CJ. Thus we compared ORP5 localization to Sec61β, a subunit of the
306 Sec61 complex involved in protein translocation in the ER, that is present in ER
307 elements distributed throughout the cells and very little at ER-mitochondria contact
308 sites (Galmes et al. 2016). Co-immunolabeling of EGFP-ORP5 or EGFP-Sec61β and
309 protein disulfide isomerase (PDI) to stain the ER, confirmed ORP5 localization in ER
310 elements close to CJ (arrow, Fig. 3c) but not of Sec61β, the bulk of which localized
311 on ER membranes distant from the CJ (0% within 0-100nm and 69% >200nm
312 distance) even when close to mitochondria (Fig. 3b and arrowheads in Fig. 3c).
313 Hence, our results support the conclusion that ORP5 specifically localizes to ER-
314 mitochondria contact sites closely associated to CJ. Interestingly, in yeast, CJ were
315 shown to be closely associated to OMM-IMM contact sites tethered by the MICOS
316 complex (Harner et al., 2011). IEM analysis using Mitofilin-EGFP, an EGFP-tagged
317 construct of the human orthologue of the central component of the MICOS complex,
318 confirmed that human Mitofilin, similarly to its yeast orthologue, preferentially
319 localizes to the IMM in close proximity of CJ and in the cristae that arise from them
320 (arrow, Fig. 3a). These results suggest that ER-mitochondria contact sites where
321 ORP5 localizes could be physically connected to the intra-mitochondrial membrane
322 contact sites near CJ.

323 To identify specific binding partners of ORP5 at ER-mitochondria contact sites
324 we carried out a MS-analysis on GFP-pull downs from cells expressing EGFP-ORP5,
325 EGFP-ORP5ΔPH (an ORP5 mutant lacking the PM-targeting PH domain that is

326 localized at ER-mitochondria but not at ER-PM contact sites), or EGFP alone as a
327 control (Fig. 4a). As expected, the highest hit detected in both EGFP-ORP5 and
328 EGFP-ORP5ΔPH pull-downs was its binding partner ORP8, with which ORP5 forms
329 a complex at contact sites including MAMs (Chung, Torta et al., 2015, Galmes et al.,
330 2016). Other major hits comprise several outer mitochondrial membrane proteins
331 (listed in Fig. 4a), including the mitochondrial outer membrane protein PTPIP51, a
332 previously reported interacting partner of ORP5 (Galmes et al., 2016).

333 Interestingly, among these proteins the Sorting Assembly Machinery Subunit 50
334 (SAM50), a central component of the SAM protein complex involved in the import
335 and assembly of mitochondria β-barrel proteins in the OMM (Hohr et al., 2018), had
336 one of the highest scores. SAM50 is part of the Mitochondrial intermembrane space
337 bridging (MIB) complex, composed of metaxin-1, metaxin-2 and the MICOS complex
338 that anchors the OMM to the IMM at CJ (Huynen et al., 2016, Ott et al., 2015).
339 SAM50 is also known to directly bind the central component of the MICOS complex
340 Mitofilin (Ott et al., 2015). Consistently, Mitofilin was also detected in the MS of
341 EGFP-ORP5 and EGFP-ORP5ΔPH pull-downs (Fig. 4a). Interestingly, SAM50 and
342 Mitofilin showed a higher interaction score in EGFP-ORP5ΔPH immunoprecipitates,
343 as compared to EGFP-ORP5. Of note, metaxin-2, another component of the MIB
344 complex, localized to the outer mitochondrial membrane, was also detected in the
345 MS of immunoprecipitated EGFP-ORP5ΔPH, whereas its score in the EGFP-ORP5
346 was lower than the assigned threshold (50) (Fig. 4a). To verify that the
347 overexpression of ORP5 or ORP5ΔPH did not affect the protein levels of SAM50 and
348 Mitofilin, WB analysis using anti-actin as loading control was carried out on cells
349 expressing EGFP-ORP5, EGFP-ORP5ΔPH or EGFP alone. Our results show that
350 neither EGFP-ORP5 nor EGFP-ORP5ΔPH overexpression alters the amount of

SAM50 and Mitofilin proteins as compared to the overexpression of EGFP alone (Fig. S2b).

To confirm ORP5/8 interaction with SAM50 and Mitofilin, GFP-pull down experiments from HeLa cells expressing EGFP-ORP5, EGFP-ORP8 or EGFP alone were carried out (Fig. 4b). Consistent with the MS data, endogenous SAM50 and Mitofilin were recovered with both EGFP-ORP5 and EGFP-ORP8 but not with EGFP alone, confirming specific interaction of ORP5 and ORP8 with SAM50 and Mitofilin. Of interest, the interaction of SAM50 and Mitofilin with EGFP-ORP5 was stronger than with EGFP-ORP8. To visualize the sites of this interaction we performed confocal imaging of HeLa cells transfected with EGFP-ORP5 and stained with anti-Mitofilin antibody, as Mitofilin is the major component of the MICOS complex. We observed strong co-localization of non-cortical ORP5-labeled ER elements (MAMs) and Mitofilin-enriched microdomains on mitochondria (Fig. 4c and S2a), further confirming the physical association of ORP5 and the MIB/MICOS complex at ER-mitochondria contact sites.

Next, to determine the domains involved in the interaction of ORP5 with the MIB/MICOS complex GFP-pull down experiments were carried out from cells expressing EGFP-tagged ORP5 (EGFP-ORP5ΔPH) or ORP8 (EGFP-ORP8ΔPH) PH domain deleted constructs, and compared to the full-length proteins (EGFP-ORP5 and EGFP-ORP8) or to the EGFP alone. In accord with the MS data, the deletion of the PH domain increased ORP5 interaction with SAM50, as compared to the full-length protein (Fig. 4d). In addition, EGFP-ORP8ΔPH interaction with SAM50 was higher than of EGFP-ORP8, although still lower than the interaction of EGFP-ORP5ΔPH or even EGFP-ORP5 with SAM50.

375 As the PH domain is not required for the interaction with SAM50 we further
376 investigated the role of the other domains of ORP5 in such interaction by
377 immunoprecipitating ORP5 deletion mutants for the ORD and the transmembrane
378 (TM) domains (EGFP-ORP5ΔORD, EGFP-ORP5ΔTM). While the deletion of the
379 ORD domain did not affect the interaction between ORP5 and SAM50, the deletion of
380 the TM domain decreased the amount of SAM50 co-immunoprecipitated with ORP5,
381 indicating that ORP5 should be properly anchored to the ER to localize at ER-
382 mitochondria contact sites and to interact with SAM50 (Fig. 4d).

383 To observe ORP5 and SAM50 localization we performed confocal analysis on
384 cells expressing EGFP-ORP5 or EGFP-ORP5ΔPH and stained with an anti-SAM50
385 antibody to look at the endogenous protein (Fig. 4e). As expected, endogenous
386 SAM50 localizes on mitochondria in cells stained with Mitotracker and, as previously
387 shown (Galmes et al., 2016), EGFP-ORP5 localizes to both ER-PM and ER-
388 mitochondria contact sites while the EGFP-ORP5ΔPH loses its localization to ER-PM
389 contacts. Both full-length and ΔPH constructs co-localized with endogenous SAM50
390 at ER elements in contact with mitochondria (Fig. 4e). However, this was more
391 evident in the case of EGFP-ORP5ΔPH (bottom image, Fig. 4e).

392 Since ORP5 is not detectable at endogenous levels by microscopy, to assess
393 ORP5 and SAM50 localization when both proteins are expressed at similar levels, we
394 generated a C-terminally tagged construct of SAM50 (SAM50-HA) and co-expressed
395 this construct with EGFP-tagged full-length ORP5 or ORP8 and ΔPH mutant
396 constructs. First, we verified that SAM50-HA was properly localized to mitochondria
397 by confocal microscopy (Fig. S2c). Then we co-expressed SAM50-HA together with
398 EGFP-ORP5, EGFP-ORP5ΔPH or EGFP-ORP5is2 (a natural variant of ORP5
399 deleted of most of its PH domain, K134-V201) (Fig. S2d, S2e, S2f) and in parallel

experiments with EGFP-ORP8 or EGFP-ORP8ΔPH (Fig. S3a, S3b) in HeLa cells and analyzed their localization by confocal microscopy. ORP5-containing ER elements were found in close proximity to SAM50-stained mitochondria. This effect was more prominent in the case of EGFP-ORP5ΔPH or EGFP-ORP5is2 (Fig S2e, S2f), but less evident in the case of EGFP-ORP8 or EGFP-ORP8ΔPH (Fig. S3a, S3b), consistent with the stronger interaction of ORP5 with SAM50 as compared to ORP8. However, we did not observe a shift in the localization of ORP5 from the cortical ER (in the case of full-length ORP5/8) or from the reticular ER (in the case of ORP5/8 ΔPH) to the non-cortical ER in close proximity to mitochondria, as previously shown for both ORP5 and ORP8 when co-expressed with PTPIP51 (Galmes et al 2016). This might be explained by the fact that, while PTPIP51 is a tethering protein that expands ER-mitochondria contact sites when overexpressed, SAM50 does not function as an ER-mitochondria tether.

To test whether the interaction of ORP5 with the MIB complex could facilitate the non-vesicular transfer of PS from the ER to the mitochondrial membranes (and consequently synthesis of mitochondrial PE) we depleted ORP5, SAM50 or Mitofilin alone or in combination by RNAi and analyzed the content in mitochondrial PE newly synthesized from PS using the same radiometric PS-to-PE conversion assay *in situ* described above. Robust knockdown of ORP5, SAM50 or Mitofilin was confirmed by western blotting after 48 hours (Fig. 5a). Analysis of PS-derived newly synthetized PE revealed a significant decrease in PE in ORP5 (Fig. 1d and Fig. 3b) and Mitofilin knockdown cells (Fig. 5b). Moreover, the double-knockdown of ORP5 and Mitofilin had an additive effect, supporting a cooperation of these two proteins in the same process (PS transport/PE synthesis). However, the levels of PE were not changed in SAM50

425 knockdown cells as compared to control. This can be explained by the fact that
426 other subunits of the MIB complex (i.e. Mitofilin) might compensate for its
427 depletion. Indeed, levels of Mitofilin are increased in SAM50 knockdown cells (Fig.
428 5a). Accordingly, the double-silencing of SAM50 and either ORP5 or Mitofilin had
429 a significant impact on PE synthesis (Fig. 5b). Moreover, the reduction in PE was
430 even stronger as compared to the individual knockdowns indicating that disruption
431 of both a component implicated in a direct transport of PS at ER-mitochondria
432 contact sites and a component of the OMM-IMM tethering complex has a
433 significant impact on PE synthesis.

434 To verify the possibility of an indirect effect of Mitofilin or SAM50 silencing on the
435 morphology and abundance of ER-mitochondria contacts we carried out a
436 morphological analysis by conventional EM in all these knockdown conditions and
437 quantified ER-mitochondria contacts by HRP-KDEL EM (to stain the ER) in Mitofilin
438 or SAM50 silenced cells. Morphological analysis by conventional EM showed that
439 transient (48 hours) knockdowns of SAM50 and Mitofilin, as well as double-
440 knockdowns of ORP5+Mitofilin, ORP5+SAM50 and SAM50+Mitofilin, induce
441 formation of multilamellar cristae, almost devoid of CJ (Fig. S4a-b), complementing
442 previous observations obtained by other groups through stable disruption of the
443 MICOS/MIB functions (Ding, Wu et al., 2015, Ott et al., 2015). However, in all
444 knockdown conditions analyzed ER-mitochondria contact sites were still present and
445 their morphology not altered. Quantitative morphological analysis by HRP-KDEL EM
446 in control and Mitofilin or SAM50 silenced cells confirmed that the abundance of ER-
447 mitochondria contact sites was not altered by Mitofilin or SAM50 knockdown (Fig. 5c-
448 d) indicating that the effects on PS-derived PE synthesis were specifically due to
449 Mitofilin or SAM50 loss of function effects on intra-mitochondrial membrane bridges.

450 Overall our results indicate that ER-mitochondria contacts where ORP5/8 localize
451 are physically linked to intra-mitochondria contacts where the components of the
452 MIB/MICOS complex reside, and this association facilitates the transfer of PS from
453 the OMM to the IMM for synthesis of PE.
454
455 **ORP5 additionally regulates VDAC-mediated Ca^{2+} import to mitochondria by**
456 **acting on the MIB component SAM50**
457 To get further insights into the functional link between ORP5/8 and the
458 MIB/MICOS complex we explored whether ORP5 and ORP8 knockdowns might
459 affect the expression and/or the localization of SAM50 and Mitofilin. Interestingly
460 when we analyzed cell lysates by WB, we found that SAM50 and Mitofilin protein
461 expression was significantly and specifically increased in ORP5- but not in ORP8
462 knockdown cells, as compared to control cells (Fig. 6a-b). The effects of ORP5
463 silencing were specific for SAM50 and Mitofilin, as other mitochondrial proteins
464 (Cytochrome c, CV-ATP5A) or proteins of the general ER (PDI) and of the MAMs
465 (VAPB) were not affected (Fig. S5a). This could also be observed by IF analysis
466 where the increase in SAM50 staining on mitochondria is specific to ORP5
467 knockdown (Fig. 6c, S5b-c).
468 Intriguingly, such increase in SAM50 was accompanied by a dramatic
469 accumulation in the voltage-dependent anion channel VDAC, a 19-stranded
470 transmembrane β-barrel protein (Colombini, 2012) that requires SAM50 for its
471 biogenesis and insertion in the OMM (Hohr et al., 2018). These results suggest that the
472 accumulation of VDAC protein in ORP5 knockdown cells is due to the parallel
473 increase of SAM50. Indeed, overexpression of SAM50-HA in control HeLa cells was
474 sufficient to induce an increase in endogenous VDAC (Fig. S5d). Also, the

475 simultaneous knockdowns of ORP5 and SAM50 rescued the increase in VDAC,
476 confirming that its accumulation in ORP5 knockdown cells was due to the
477 accumulation of SAM50. Interestingly, ORP5 and SAM50 double-knockdown did not
478 rescue the increased protein levels of Mitofilin (Fig. 6a-b), in accord with the fact that
479 SAM50 knockdown alone also increased the protein levels of Mitofilin. To verify that
480 the increase in their protein amounts did not depend on the increase in their
481 transcripts we quantified the transcript levels of ORP5, SAM50 and the three VDAC
482 isoforms (VDAC1, 2 and 3) by real-time PCR upon ORP5 or SAM50 knockdown (Fig.
483 6d, S5e). The quantity of SAM50 and Mitofilin transcripts was unaffected by ORP5
484 silencing, and VDAC1 transcript levels were even slightly reduced, possibly reflecting
485 a compensatory mechanism induced by the increase in VDAC protein. Similarly,
486 VDAC and Mitofilin transcript levels were not affected in the absence of SAM50,
487 although transcript levels of ORP5 were increased, possibly reflecting a regulatory
488 mechanism controlled by the levels of SAM50. Overall, these data indicate that
489 ORP5 knockdown induces an accumulation of SAM50 and VDAC (SAM50-
490 dependent) proteins in the absence of major effects on the corresponding mRNAs.

491 To confirm that the accumulation of SAM50-VDAC was indeed due to ORP5
492 function at ER-mitochondria contact sites and not from indirect effects of ORP5 at
493 ER-PM contacts we re-expressed EGFP-ORP5is2 (a ORP5 isoform lacking the PH
494 domain and thus localized at MAMs but not at ER-PM contacts) in Ctrl and ORP5
495 knockdown cells and analyzed the protein levels of SAM50 and VDAC by WB (Fig.
496 6e). As a control EGFP alone was transfected. A complete rescue of SAM50 and
497 VDAC levels was observed in ORP5 knockdown cells transfected with EGFP-
498 ORP5is2 but not in cells transfected with the EGFP alone. These results confirmed

499 that the increase in SAM50 and VDAC was the effect of the specific loss of function
500 of ORP5 at MAMs.

501 Given the role of ORP5 in regulating levels of mitochondrial PE, it is possible that
502 the increase in SAM50, and consequently of VDAC, observed in ORP5 knockdown
503 cells is linked to the decrease in PE on mitochondria membranes. Thus, we
504 investigated if reducing the levels of mitochondrial PE by knocking down the PS-
505 decarboxylase PISD, enzyme that converts PS in PE in mitochondria, induces a
506 similar increase in SAM50-VDAC proteins (Fig. 6f). WB analysis confirmed robust
507 suppression of PISD and an increase in SAM50 and VDAC, similarly to that observed
508 upon ORP5 knockdown. These data strongly suggest that the decrease of PE in
509 ORP5 depleted cells is responsible for the abnormal stabilization of SAM50 and
510 VDAC in mitochondrial membranes. They also strengthen the importance of having
511 proper levels of PE to ensure correct turnover and function of mitochondrial protein
512 complexes.

513 As VDAC is one of the major mitochondrial players in mediating Ca^{2+} transport
514 and signaling between ER and mitochondria (Rapizzi, Pinton et al., 2002), we next
515 investigated if ORP5 knockdown could regulate Ca^{2+} influx from the ER to
516 mitochondria in living cells. We first used a ratiometric Ca^{2+} indicator selectively
517 targeted to mitochondria (mt-Pericam) which is based on a circularly permuted yellow
518 fluorescent protein fused to calmodulin (Nagai, Sawano et al., 2001). Upon binding to
519 Ca^{2+}, the excitation peak of mt-Pericam shifts from 415 nm to 494 nm while the
520 emission spectrum remains unchanged around 515 nm, allowing us to quantify rapid
521 changes in mitochondrial Ca^{2+}. We thus transfected ORP5, ORP8 or Ctrl siRNA-
522 treated cells with mt-Pericam and then measured mitochondrial Ca^{2+} fluxes, in
523 response to histamine, by live-cell spinning disk microscopy (Fig. 7a-b). Soon after

524 the addition of histamine, mt-Pericam fluorescence ratio (488/405) rapidly increased
525 in all conditions, reflecting the increase in mitochondrial Ca^{2+} influx triggered by the
526 histamine treatment. However, interestingly, ORP5 knockdown cells showed a
527 significantly higher increase as compared to ORP8 knockdown and to control cells.
528 Quantification of the maximum amplitude of the response after histamine treatment
529 (expressed as R_{max}/R_0, where R is the 488/405 ratio, R_{max} is the maximum
530 fluorescence ratio after histamine addition and R_0 the basal ratio before histamine
531 addition) confirmed that ORP5 but not ORP8 silencing induced a statistically relevant
532 increase of mitochondrial Ca^{2+} influx, triggered by the addition of histamine, as
533 compared to control cells (Fig. 7b).

534 Passive entry of Ca^{2+} into mitochondria can be driven by large negative
535 membrane potential of mitochondria and occurs through the mitochondrial Ca^{2+}
536 uniporter MCU spanning the IMM (Patron, Raffaello et al., 2013). To be sure that the
537 increase of mitochondrial Ca^{2+} upon ORP5 knockdown was not indirectly due to a
538 change of mitochondrial membrane potential, we performed flow cytometric analysis
539 in ORP5 or ORP8 knockdown cells. Knockdown cells were loaded with the
540 mitochondrial membrane potential sensitive dye TMRE (Tetramethylrhodamine ethyl
541 ester), in the presence (or absence) of the mitochondrial oxidative phosphorylation
542 uncoupler CCCP (Carbonyl cyanide 3-chlorophenylhydrazone) to induce membrane
543 depolarization (Fig. S6a). Neither ORP5 nor ORP8 knockdown altered mitochondrial
544 membrane potential as compared to control cells, even in presence of CCCP that
545 strongly decreases TMRE fluorescence intensity (Fig. S6a), showing that the effect of
546 ORP5 knockdown on Ca^{2+} is not due to a change of mitochondrial membrane
547 potential.

548 To further study the role of ORP5 in the regulation of Ca^{2+} homeostasis a parallel
549 set of experiments was performed using another type of Ca^{2+}-probe, the red
550 fluorescent genetically encoded Ca^{2+} indicator (R-GECO) and its two variants
551 selectively-targeted to mitochondria (mito-LAR-GECO) or ER (ER-LAR-GECO) to
552 respectively measure cytosolic, mitochondrial and ER Ca^{2+} in living cells (Fig. 7c-e).
553 These experiments confirmed that ORP5 silencing increases mitochondrial Ca^{2+}
554 uptake (Fig. 7c). The increase in mitochondrial Ca^{2+} uptake triggered by histamine
555 treatment was accompanied by a decrease in ER Ca^{2+} and an increase in cytosolic
556 Ca^{2+} in all conditions (Fig. 7d-e). Interestingly, no statistically relevant differences of
557 the decrease ER Ca^{2+} were measured between ORP5 silenced and control cells.
558 This indicates that the effects on mitochondrial Ca^{2+} fluxes observed in ORP5 do not
559 depend on the modification of ER Ca^{2+} storage or release. An increase in cytosolic Ca^{2+}
560 was measured in ORP5 and ORP8 silenced cells as compared to control. As this
561 increase was not specific for ORP5 silencing, it likely reflects a common role of
562 ORP5/8 in Ca^{2+} homeostasis at ER-PM contact sites, as recently proposed (Pulli,
563 Lassila et al., 2018).
564 So far, our data show that the absence of ORP5 increases mitochondrial Ca^{2+}
565 possibly by acting on the mitochondrial proteins SAM50 and VDAC, supported by the
566 specific accumulation of these two proteins in the absence of ORP5. To confirm that
567 the increase of mitochondrial Ca^{2+} in ORP5-silenced cells was indeed dependent on
568 VDAC and SAM50, we measured mitochondrial Ca^{2+} using mt-Pericam in VDAC- (all
569 three isoforms), ORP5+VDAC- and ORP5+SAM50- doubly-silenced cells. A
570 significant decrease in VDAC and SAM50 as well as ORP5 levels was detected by
571 WB in the corresponding silenced cells (Fig. 8a and Fig. 6a). Even though the
572 increased level of VDAC protein induced by the absence of ORP5 was not

573 completely rescued in ORP5+VDAC or ORP5+SAM50 knockdowns, the increase in
574 mitochondrial Ca^{2+} phenotype was significantly rescued to control levels and partially
575 rescued in ORP5+VDAC and ORP5+SAM50-silenced cells, respectively (Fig. 8b and
576 c). Overall, these results demonstrated that ORP5 plays an additional role in
577 regulating import of mitochondrial Ca^{2+} through regulation of SAM50 and VDAC
578 proteins.
579

580 **ORP5 knockdown induces cell senescence in a SAM50-dependent manner**

581 Accumulation of mitochondrial Ca^{2+} has been shown to be involved in both
582 apoptotic cell death and senescence (permanent cell proliferation arrest) (Wiel,
583 Lallet-Daher et al., 2014). Interestingly, it has also been shown that ORP5 expression
584 promotes cell proliferation (Du, Zadoorian et al., 2018). As our data show a new role
585 of ORP5 in regulating Ca^{2+} import to mitochondria at ER-mitochondria contact sites
586 (Fig. 8), we were wondering if ORP5 could mediate cellular processes such as
587 apoptosis and senescence. To address this question, we decided to study both
588 apoptosis and senescence in ORP5 depleted cells.

589 For apoptosis, we performed immunofluorescence and stained with anti-cleaved
590 caspase-3 (to detect apoptotic cells) HeLa cells transfected with control siRNA or
591 siRNA against ORP5 or ORP8. We also treated the knockdown cells with
592 staurosporine to induce apoptosis or with DMSO as vehicle control (Fig. S4b).
593 Quantification of the percentage of cleaved caspase-3 positive cells (% of total cells)
594 in all conditions showed no significant difference between ORPs knockdown and
595 control cells (Fig. S6b), even in presence of staurosporine, showing that in these
596 conditions transient silencing of ORP5/8 does not induce apoptosis.

597 To study cellular senescence we performed knockdown of ORP5 in MRC5
598 normal human fibroblasts that are a good model for senescence studies (Ma,
599 Warnier et al., 2018). We first looked at cell proliferation using crystal violet staining
600 in both control and ORP5 knockdown cells (Fig. 9a). A significant decrease of the cell
601 number was detected in ORP5 depleted cells compared to control (Fig. 9a). This
602 decrease of the cell number in ORP5 knockdown cells could be correlated with an
603 increase of the Senescence-associated β –galactosidase (SA β-gal) staining as
604 compared to control (Fig. 9a). Accordingly, these results were corroborated by qRT-
605 PCR analysis showing a significant increase of the senescence markers p16 and p21
606 and a significant decrease of the proliferation marker Ki67 in ORP5 knockdown cells
607 compared to control (Fig. 9b). Because we have shown that ORP5 knockdown
608 induces an elevation of mitochondrial Ca^{2+} via a SAM50-dependent accumulation of
609 VDAC, we hypothesized that the induction of senescence in MRC5 cells could also
610 be due to the effect of ORP5 on SAM50. Thus, we decided to perform a double-
611 knockdown of ORP5 and SAM50 in MCR5 cells. In accord with our hypothesis, this
612 double-silencing partially rescued the senescence phenotype found in ORP5
613 knockdown cells. ORP5+SAM50 double-knockdown cells displayed increased
614 proliferation and underwent less senescence as compared to ORP5 single
615 knockdown cells (Fig. 9c). To verify that this effect on cellular senescence was
616 specific to ORP5, given its role in mitochondria Ca^{2+} regulation, we performed in
617 parallel a knockdown of ORP8 in MRC5 cells. Differently to ORP5, ORP8 knockdown
618 did not induce cell senescence (Fig. 9c). Taken together, these data reveal a novel
619 specific role of ORP5, involving SAM50, in regulating the cellular senescence in
620 MRC5 cells.
621

622 **DISCUSSION**

623 In this study, by using a combination of *in vitro* and *in situ* biochemical and imaging
624 approaches, we describe a new function of ORP5/8 in the maintenance of mitochondrial
625 levels of PE, an essential phospholipid of mitochondria, in mammalian cells. Importantly,
626 we provide the first evidence of LTPs (ORP5 and ORP8) directly mediating non-
627 vesicular transfer of PS at ER-mitochondria contact sites, from the ER to the
628 mitochondria where it is converted into PE.

629 In yeast, large tethering complexes such as the ERMES and the ER-Membrane
630 protein Complex (EMC) have been previously involved in phospholipid trafficking (PC
631 and PS, respectively) between the ER and the mitochondrial membranes (Tamura &
632 Endo, 2017) (Lang, John Peter et al., 2015). For instance, three subunits of the
633 ERMES complex contain a Synaptotagmin-like Mitochondria lipid binding Protein
634 (SMP) domain that forms a hydrophobic lipid transport cavity shared by other
635 proteins of the tubular lipid-binding protein TULIP superfamily (Kopec, Alva et al.,
636 2010, Reinisch & De Camilli, 2016). However, a direct role (independent of its
637 tethering function) of ERMES in lipid transport at ER-mitochondria contact sites is still
638 questioned. For a long time homologues of the ERMES complex have not been
639 identified in metazoan. Hirabayashi et al. recently showed that the SMP-containing
640 protein PDZD8 is involved in ER-mitochondria tethering and in the regulation of Ca^{2+}
641 dynamics in mammalian neurons (Hirabayashi et al., 2017). Although PDZD8 is a
642 structural and functional paralogous of the Mmm1 subunit of the ERMES complex
643 (Wideman, Balacco et al., 2018), its function in lipid transport at ER-mitochondria
644 contact sites remain unclear. The EMC complex, which has been involved in PS
645 shuttling at ER-mitochondria contact sites in yeast, is instead highly conserved in
646 metazoans (Wideman, 2015). However, no lipid-binding/transfer domain has been

647 found in the EMC proteins, indicating that their implication in lipid transfer at ER-
648 mitochondria contacts is linked to their tethering function rather than to a direct lipid
649 transfer activity. Recently, the mammalian LTP VPS13A has been shown to localize
650 to contact sites including ER-mitochondria contacts (Kumar et al., 2018). VPS13A
651 contains a lipid-binding domain (VPS13α) that has the ability to harbor multiple
652 phospholipids at once and transfer them between liposomes *in vitro*. However, its
653 role in lipid transfer at membrane contact sites *in situ* has not yet been established.
654 Differently from the SMP and VPS13α that can simultaneously host multiple
655 phospholipids, the ORD domain of Osh/ORPs forms a cavity that can host only one
656 lipid at a time (Maeda, Anand et al., 2013, Wang, Ma et al., 2019).

657 ORP5 and ORP8 have recently been shown to counter-exchange PS with the PM
658 phosphoinositides PI4P and PIP_2 at ER-PM contact sites in HeLa cells (Chung et al.,
659 2015, Ghai, Du et al., 2017). However, PI4P and PIP_2 are not present on the
660 mitochondrial membranes, while PE is highly abundant in these membranes, in
661 addition to being an essential lipid of all biological membranes. Our *in vitro* data show
662 that the ORD domains of ORP5 and ORP8 transport PS, but not other phospholipids
663 such as PE and PC, indicating a specific role of ORP5/8 in PS transport and excluding
664 the possibility that ORP5/8 might also participate in the transport of a fraction of PE
665 back to the ER. It is possible that ORP5/8 cooperate with other LTPs, such as VPS13A,
666 for the exchange of other lipids (including PE) at ER-mitochondria contact sites.
667 Importantly, we have confirmed the role of ORP5/8 in PS transfer by measuring a
668 decrease of PS-derived mitochondrial PE in ORP5 depleted HeLa cells *in situ* (and
669 even more upon ORP5+8 silencing, although the effect of ORP5 depletion was
670 predominant as compared to ORP8) as well as a reduction of total PE in
671 mitochondria isolated from these cells (Fig. 1c-f). Accordingly, the knockdown of

672 ORP5/8 affects cristae morphology (Fig. 2a, 2c) and the respiratory function of
673 mitochondria (Galmes et al., 2016)(Fig. 2d), all phenotypes that are expected in the
674 case of decrease in mitochondrial PE (Joshi et al., 2012, Steenbergen et al., 2005).
675 Our data further confirm the essential role of PE in the maintenance of mitochondria
676 structure and functions, and are in accord with those of (Tasseva et al., 2013)
677 showing that even a mild decrease of mitochondrial PE can strongly alter
678 mitochondria cristae morphology and respiratory function. Our data also suggest that
679 the gradient of PS at ER-mitochondria contacts is sufficient to trigger the ORP5/8-
680 mediated unidirectional transport of PS from the MAMs, where it is highly enriched, to
681 the mitochondria membranes, where it is rapidly converted into PE and is therefore
682 present at a very low amount. Our findings have important implications in the general
683 field of LTPs, as they suggest that the same LTP can use different means to transfer
684 lipids depending on the local gradients present at the specific membrane contact
685 sites where it is localized. They also suggest a possible new function in PS transport at
686 ER-mitochondria contact sites for the yeast orthologues of ORP5/8, Osh6/7p, whose
687 localization/function at ER-mitochondria contact sites still remain to be addressed
688 (Moser von Filseck, Copic et al., 2015).

689 Another important feature of our work is the observation that ORP5 and ORP8
690 knockdowns do not affect the extent of ER-mitochondria contact sites. These data,
691 consistent with our previous observation that ORP5/8 overexpression does not alter
692 the length of ER-mitochondria contacts (Galmes et al., 2016), confirm that the main
693 function of these proteins at MAMs is lipid transfer and not membrane tethering. This
694 is a unique feature among the LTPs that have been identified so far at MAMs. For
695 instance, modulation of the protein levels of other LTPs such as ERMES in yeast, or
696 PDZD8 and VPS13A in mammals, results in an alteration of the extent of ER-

697 mitochondria contact sites (Hirabayashi et al., 2017, Kornmann, Currie et al., 2009,
698 Kumar et al., 2018). Thus, ORP5/8 represent so far a unique tool to study lipid
699 transport at ER-mitochondria contact sites, independently of membrane tethering.

700 Importantly, our study also reveals that ORP5/8 physically interact with SAM50
701 and Mitofilin, two key components of the MIB/MICOS complex that anchor the IMM to
702 the OMM at the level of CJ (Huynen et al., 2016, Ott et al., 2015, Wollweber et al.,
703 2017). The biochemical interaction between ORP5 and SAM50/Mitofilin suggests the
704 existence of a physical link between ER-mitochondria contact sites involved in lipid
705 transport and intra-mitochondria contacts. ORP5 localization by IEM at ER-mitochondria
706 contact sites near the CJ, where Mitofilin and MICOS complex also reside, confirms the
707 existence of such tripartite membrane structure. Importantly, we also show that the *de-*
708 *novo* synthesis of mitochondrial PE requires both the lipid transfer activity of ORP5 at
709 ER-mitochondria contact sites and the tethering activity of the MIB/MICOS complex at
710 intra-mitochondrial OMM-IMM contact sites (Fig. 5b). Interestingly, recent evidence in
711 yeast suggests that, in addition to the classical PE synthesis at the IMM by the IMM-
712 localized PS decarboxylase Psd1, PE can be also synthesized *in trans* on the OMM
713 (Aaltonen, Friedman et al., 2016). Thus, it is possible that this alternative pathway,
714 which requires MIB/MICOS tethering function to bring the mitochondrial
715 intermembrane domain of PISD close to the OMM for synthesis of PE, is conserved
716 also in mammalian cells. The cooperation of ORP5 with SAM50 and Mitofilin could
717 facilitate the movement of PS from the ER to the IMM across ER-mitochondria
718 contact sites for synthesis of PE at the IMM, through the classical PE synthesis
719 pathway, but also PISD function *in trans* on the OMM through this alternative
720 biosynthetic pathway. Taken together these findings provide the first evidence of a
721 physical link between ER-OMM and OMM-IMM contact sites to facilitate transport of

722 PS from the ER to the mitochondria and PE synthesis on the mitochondrial
723 membranes (Fig. 10).

724 Finally, we uncover a specific role for ORP5, but not ORP8, in regulating
725 mitochondrial Ca^{2+} uptake, via a SAM50-VDAC axis. SAM50, in addition to being part
726 of the MIB complex, is also the major subunit of the Sorting and Assembly Machinery
727 (SAM) that mediates membrane insertion and assembly of mitochondrial β-barrel
728 proteins (Hohr et al., 2018, Kozjak et al., 2003). One of the most abundant
729 mitochondria β-barrel proteins is VDAC, which forms a pore that allows the passage of
730 small metabolites and ions such as ATP and Ca^{2+} across the OMM (Colombini, 2012).
731 VDAC exists as three isoforms (VDAC1, 2 and 3) that share common channeling
732 properties. VDAC interacts with the IP3Rs located in the ER membrane via the
733 molecular chaperone GRP75 that links the two proteins together. The interaction
734 between IP3Rs and VDACs acts as a bridge to allow the transfer of Ca^{2+} from the ER to
735 the OMM, and then from the OMM to the mitochondrial matrix through the mitochondrial
736 Ca^{2+} uniporter MCU. Ca^{2+} release from the ER to mitochondria is triggered by IP_3
737 binding to IP3Rs upon histamine treatment (Rizzuto, Marchi et al., 2009). Here we show
738 that knockdown of ORP5 increases the protein levels of SAM50 and VDAC as well as
739 the levels of histamine-induced Ca^{2+} import to mitochondria. We also confirm that the
740 additional role of ORP5 in regulating SAM50-VDAC levels is not indirectly due to ORP5
741 function at ER-PM contacts as re-expression of an ORP5 deletion mutant that has lost
742 its localization to ER-PM contact sites completely rescues the levels of SAM50-VDAC.
743 Intriguingly, our data support the hypothesis that this novel function of ORP5 in
744 regulating levels of SAM50 and VDAC (and consequently mitochondrial Ca^{2+} uptake)
745 could be dependent on its direct function in mediating PS transport to mitochondria for
746 synthesis of mitochondrial PE. This is consistent with the lack of effect of ORP8

747 knockdown (that alone does not induce a significant decrease in mitochondrial PE) on
748 SAM50-VDAC and mitochondrial Ca^{2+} levels and with the increase in SAM50-VDAC
749 levels in cells knocked down for PISD, the enzyme that converts PS in PE on
750 mitochondria. The present data are also in accord with a previous work showing that
751 lack of mitochondrial PE by depleting Psd1/2 in yeast induced stabilization and even
752 appearance of higher forms of respiratory chain supercomplexes (Bottinger, Horvath
753 et al., 2012). Importantly, double-knockdown of ORP5 and VDAC rescues the
754 mitochondrial Ca^{2+} increase induced by ORP5 silencing, confirming that this increase in
755 Ca^{2+} is indeed VDAC-dependent. Mitochondrial membrane potential has been proposed
756 to influence VDAC open-closed state and consequently import of Ca^{2+} to mitochondria
757 (Tan & Colombini, 2007). However, we did not detect any alteration in mitochondria
758 membrane potential in ORP5 knockdown cells, supporting our idea that the increase in
759 mitochondrial Ca^{2+} observed in ORP5-silenced cells results from the increase in VDAC
760 protein levels. This is also in accord with previous studies showing that the
761 overexpression of VDAC in HeLa cells enhances mitochondrial Ca^{2+} uptake upon
762 histamine treatment (Rapizzi et al., 2002). Our data also indicate that the effect of
763 VDAC accumulation on mitochondrial Ca^{2+} fluxes does not depend on the modification
764 of ER Ca^{2+} storage or release. Indeed, we observed a similar decrease of ER Ca^{2+} in
765 ORP5 depleted and control cells, upon histamine treatment. Our results correlate well
766 with those of others (Rapizzi et al., 2002) who also observed a similar decrease of ER
767 Ca^{2+} in VDAC-overexpressing and control cells.

768 Accumulation of Ca^{2+} in mitochondria, induced by release of Ca^{2+} from the ER
769 through IP3R channel, was recently shown to be involved in cellular senescence in
770 normal cells (Martin & Bernard, 2018, Wiel et al., 2014). Interestingly, we found that
771 knockdown of ORP5, but not ORP8, induces cellular senescence in MCR5 cells.

772 These findings are highly relevant because ORP5 overexpression has been
773 associated with several tumors (Du, Turner et al., 2017). We also show that double-
774 knockdown of ORP5 and SAM50 restores the levels of VDAC protein, as well as of
775 mitochondrial Ca^{2+}, and enables cells to escape the senescence induced by ORP5
776 depletion. These data confirm that all the above phenotypes are dependent on SAM50,
777 and possibly on its known role in the biogenesis of VDAC (Hohr et al., 2018). Future
778 studies are required to further dissect the mechanisms underlying the role of ORP5 in
779 modulating SAM50 protein levels in mitochondria.

780 In conclusion, our data reveal that: 1) ORP5/8 constitute the molecular machinery
781 mediating PS transfer at ER-mitochondria contact sites but not ER-mitochondria
782 tethering; 2) ER-mitochondria contacts where ORP5/8 localize are physically associated
783 with intra-mitochondrial contacts to facilitate the transport of PS from the ER to
784 mitochondria membranes; 3) ORP5 plays a novel specific role in regulating
785 mitochondrial Ca^{2+} fluxes at ER-mitochondria contact sites via SAM50/VDAC (Fig. 8)
786 and cellular senescence in MCR5 cells. Our study uncovers a novel link between lipid
787 and Ca^{2+} transport at ER-mitochondria contact sites and provides a first molecular clue
788 on how lipids are transported at ER-mitochondria contact sites. Furthermore, we
789 reveal a specific role of ORP5 in regulating mitochondrial Ca^{2+} homeostasis and
790 cellular senescence in mammalian cells.

791

792

793

794

795

796

797 **METHODS**

798 **Cell culture, siRNA and transfection**.

799 HeLa cells were cultured in DMEM (Life Technologies) containing GlutaMax (Life
800 Technologies) and supplemented with 10% FBS (Life Technologies) and 1%
801 penicillin/streptomycin (Life Technologies) at 37°C and 5% CO_2. Transfection of
802 plasmids and siRNA oligos (Dharmacon, GE Healthcare) was carried out with
803 lipofectamine 2000 and oligofectamine (Life Technologies) according to
804 manufacturer's instructions.

805 For senescence studies, MRC5 normal human fibroblasts (ATCC) were cultured in
806 Dulbecco′s modified Eagle′s medium (Life Technologies) containing GlutaMax (Life
807 Technologies) and supplemented with 10% FBS (Sigma-Aldrich) and 1%
808 penicillin/streptomycin (Life Technologies). MRC5 were transfected with siRNAs
809 using Dharmafect 1 transfection reagent according to manufacturer's instructions
810 (Dharmacon, GE Healthcare).

811

812 **siRNAs oligonucleotides**

813 For knockdowns, HeLa cells were transfected with siRNA oligos by using
814 oligofectamine (Life Technologies) and cultured for 48 hours prior to analysis.

815 For senescence studies, MRC5 cells were transfected with siRNAs using Dharmafect
816 1 transfection reagent according to manufacturer's instructions (Dharmacon, GE
817 Healthcare).

818 Double-stranded siRNAs were derived from the following references:

siRNA	Company, Reference
OSBPL8	Dharmacon, J-009508-06 (Galmes et al., 2016)
OSBPL8	Dharmacon, J-009508-05 (Galmes et al., 2016)

OSBPL5	Dharmacon, J-009274-10 (Galmes et al., 2016)
OSBPL5	Dharmacon, J-009274-11 (Galmes et al., 2016)
SAMM50	Dharmacon, J-017871-18
SAMM50	Dharmacon, J-017871-19
Non-targeting	Dharmacon, D-001810-10
hVDAC1	5'-AAGCGGGAGCACATTAACCTG-3' (De Stefani, Bononi et al., 2012)
hVDAC2	5'-AAGGATGATCTCAACAAGAGC-3' (De Stefani et al., 2012)
VDAC3	5'-AAGGGTGGCTTGCTGGCTATC-3' (De Stefani et al., 2012)
siMitofilin	5' -AAUUGCUGGAGCUGGCCUUTT-3' (John, Shang et al., 2005)
siPISD	5' -GGAAGGGAAUGAGCUCUAUCACU -3' (si PISD "C" Origene)

Plasmids and cDNA clones

EGFP-ORP5, EGFP-ORP8, EGFP-ORP5ΔPH, EGFP-ORP8ΔPH, EGFP-ORP5ΔORD and EGFP-ORP5ΔTM were described in (Galmes et al., 2016).

The following reagents were kind gifts: GFP-Sec61β from T. Rapoport (Harward University)(Shibata, Voss et al., 2008), 2mt RP ratiometric Pericam from Paolo Pinton (University of Ferrara) (Filippin, Abad et al., 2005); ssHRP-KDEL from T. Schikorski (Schikorski, Young et al., 2007); GST-ORD8 (ORD ORP8, corresponding to aa 328-767) from P. De Camilli (Chung et al., 2015). GECO constructs were from Robert Campbell (Addgene: CMV-R-GECO1 # 32444, CMV-mito-R-GECO1 # 46021, CMV-ER-LAR-GECO1 # 61244, CMV-mito-LAR-GECO1.2 # 61245).

Cloning of HA-ORP5, HA-SAM50, Mitofilin-GFP, GST- ORD5 (ORD ORP5) and EGFP-ORP5is2

833 cDNAs of ORP5 (full-length), SAM50 (full-lenght), Mitoflin (full-length from FLAG-
834 mitofilin (Ott et al., 2015)) and GST-ORD5 (corresponding to aa 265-703), were
835 amplified by PCR. In all PCR reactions, Herculase II fusion DNA polymerase
836 (Agilent) was used. Primers used were (coding sequence shown in lowercase):
837 5' AgeI-HA-ORP5_Fw GGCGGC *ACCGGT* cgccacc ATGTACCCATACGATGTTCCA
838 GATTACGCT atgaaggaggaggccttcctc
839 3' XhoI-STOP-ORP5_Rv GGC *CTCGAG* ctatttgaggatgtggttaatg
840 5' AgeI-SAMM50_Fw GGCGGC *ACCGGT*cgccaccatggggactgtgcacgcccggagtttg 3'
841 5' XhoI-STOP-HA-SAMM50_Rv GGC*CTCGAG*ctaAGCGTAATCTGGAACATCGTAT
842 GGGTAcaggaaccttatcccagctccaaac 3'
843 5' KpnI-Mitofilin_Fw AGACCCAAGCTT *GGTACC* atg
844 3' BamHI-GC-Mitofilin_Rv GTAATC *GGATTC* GC ctctggct
845 5' SalI-TC-ORD5_Fw GCACAG GTCGAC TC gagacccctggggccccggt
846 3' NotI-STOP-ORD5_Rv GCACA *GCGGCCGC* ctactgtggccggagggctggtcg
847 For the HA-ORP5 cloning the PCR product (carrying the HA tag at the N-terminus of
848 ORP5) was ligated between AgeI and XhoI in the pEGFP-C1 vector (Clontech) and
849 replacing the GFP- with the HA-tag. For the SAMM50-HA cloning the PCR product
850 (carrying the HA tag at the C-terminus of SAM50) was ligated between AgeI and
851 XhoI in the pEGFP-C1 vector (Clontech) and replacing the GFP- with the HA-tag. For
852 the other clonings the PCR products were ligated between KpnI and BamHI for
853 Mitofilin, and between SalI and NotI for ORD5, in the pEGFP-N1 vector (Clontech) to
854 generate Mitofilin-EGFP or in the pGEX-6P-1 to generate GST-ORD5.
855 The ORP5is2, carrying a deletion (residues 134-201) in the PH domain, was
856 generated by sites directed mutagenesis using the following primers: sense 5'-
857 tggctgacagcctgaagggccccaaagg-3' and antisense 5'-cctttggggcccttcaggctgtcagcca-3'.

858 PCR was carried out using PFU ultra high fidelity (Agilent), followed by 5 hrs
859 digestion with DpnI.
860
861 **mRNA analyses by quantitative reverse transcriptase PCR (qPCR)**
862 Total RNA was isolated from HeLa cells transfected with siRNAs for 48 hours as
863 described above, by using a Purelink™ kit (Ambion/Thermo Scientific, Foster City,
864 CA). The RNA (0.5 μg per specimen) was reverse transcribed with a SuperScript
865 VILO™ cDNA synthesis kit (Invitrogen/Thermo Scientific, Carlsbad, CA) according to
866 the manufacturer's protocol. Quantification of the mRNAs of interest was carried out
867 on a Roche Lightcycler™ 480 II instrument by using SYBR-Green I Master mix
868 (Roche, Basel, Switzerland) and primers specified in Table SX. Succinate
869 dehydrogenase complex. subunit A, the mRNA of which remained markedly stable
870 under the present conditions, was employed as a reference housekeeping mRNA.
871 Relative mRNA levels were calculated by using the –ΔΔCt method.

872 Sequences of the primers used for qPCR:

mRNA	Sequence 5'-3'
SDHA* (housekeeping)	Fw: CATGCTGCCGTGTTCCGTGTGGG
	Rv: GGACAGGGTGTGCTTCCTCCAGTGCTCC
ORP5	Fw: GTGCCGCTGGAGGAGCAGAC
	Rv: AGGGGCTGTGGTCCTCGTATC
SAMM50	Fw: CAAGTGGACCTGATTTTGGAGG
	Rv: AGACGGAGCAATTTTTCACGG
Mitofilin	Fw: GTTGTATCTCAGTATCATGAGCTGG
	Rv: GTTCAGCTGATCAATACGACGA
VDAC1	Fw: ACGTATGCCGATCTTGGCAAA
	Rv: TCAGGCCGTACTCAGTCCATC
VDAC2	Fw: GCTACAGGACTGGGGACTTC
	Rv: AATGCCAAAACGAGTGCAGTT

VDAC3	Fw: GTAAATAATGCCAGCCTGATTG
	Rv: CTTCCAGGGACAAATCTGATG

873 *succinate dehydrogenase complex, subunit A

874

875 For senescence studies, MCR5 cells RNAs were extracted using RNA Extracol lysis
876 buffer (Dutscher). cDNAs were synthesized from total RNA using the Maxima first
877 strand cDNA synthesis kit (Life Technologies). Quantitative PCR mixture contained
878 cDNA, TaqMan mix (Roche), 100 µM of a Universal Probe Library probe (Roche) and
879 200 nM of primers (Sigma-Aldrich) according to manufacturer's instructions. qPCRs
880 were carried out on a FX96 Thermocycler (Bio-Rad). qPCR reactions were as
881 follows: 95°C 10 min, followed with 40 cycles of 95°C 10s, 59°C 30s. The reactions
882 were performed at least in duplicate. The relative amount of mRNA (ORP5, p16, p21,
883 Ki67, PGK1 and HPRT1) was calculated using the comparative Ct (ΔΔCt) method
884 and data were normalized using two housekeeping genes (PGK1 and HPRT1).

885

886 Sequences of the primers and UPL probes used for qPCR:

mRNA/UPL probe	Sequence 5'-3'
CDKN2A (p16) / UPL 34	Fw: GTGGACCTGGCTGAGGAG
	Rv: CTTTCAATCGGGGATGTCTG
p21(CDKN1A) / UPL 32	Fw: TCACTGTCTTGTACCCTTGTGC
	Rv: GGCGTTTGGAGTGGTAGAAAT
Ki67 / UPL 32	Fw: TCAAGGAACTGATTCAGGAGAAG
	Rv: GTGCACTGAAGAACACATTTCC
ORP5 / UPL 17	Fw: GTTGTATCTCAGTATCATGAGCTGG
	Rv: GTTCAGCTGATCAATACGACGA
PGK1 / UPL probe 67	Fw: CAGCTGCTGGGTCTGTCAT
	Rv: GCTGGCTCGGCTTTAACC
HPRT1 / UPL probe 73	Fw: TGACCTTGATTTATTTTGCATACC

	Rv: CGAGCAAGACGTTCAGTCCT

887

888

889 **Antibodies, dyes and reagents list**

890 Primary antibodies used in this study were:

	Antibody	Company & Reference
WB	IP3R-3	BD Transduction Laboratories, 610312
WB	ORP5	SIGMA, HPA038712
WB	ORP5	SIGMA, HPA058727
WB	beta-Actin	Abcam, ab8226
WB	ORP8	GeneTex, GTX121273
IF, WB	SAMM50	SIGMA, HPA034537
WB	Mitofilin	Proteintech, 10179-1-AP
WB	VDAC1	Abcam, ab15895
WB	Cytochrome C	BD Pharmingen, 556433
WB	Total OXPHOS CV-ATP5A	Abcam, ab110413
WB	PDI	GeneTex, GTX30716
WB	VAPB	SIGMA, HPA013144
WB	PSS1 (PTDSS1)	SIGMA, HPA016852
WB	PISD	SIGMA,HPA031090
IF, WB	GFP	Roche, 11814460001
IEM	GFP	Life technologies, A11122
IEM	PDI	Genetex, GTX30716
IF	HA	SIGMA, H3663
IF	Cleaved caspase-3	Cell Signaling, 9661
IF	FLAG M2	SIGMA, F1804

IF	MitoTracker® Red CMXRos	M7512, Invitrogen
IF	MitoTracker® Deep Red FM	M22426, Invitrogen
IF	HA	SIGMA, H3663
IF	Cleaved caspase-3	Cell Signaling, 9661

891

892 **Biochemical analyses**

893 ***Western blot***

894 For immunoblotting, cells were resuspended in lysis buffer [50 mM Tris, 150 mM
895 NaCl, 1% Triton X-100, 10 mM EDTA, pH 7.2, and protease inhibitor cocktail
896 (Roche)]. Cell lysates were then centrifuged at 21 000 g for 20 min at 4°C. The
897 supernatants were boiled in reducing SDS sample buffer and proteins were
898 separated using 10% SDS-PAGE and immunoblot was carried using standard
899 methods.
900 For Western blot quantification, bands of protein of interest were detected using
901 ChemiDoc™ Imaging Systems (Life Science Research, Bio-Rad) and analyzed using
902 Image Lab™ Software. All data are presented as mean ±SEM of three experimental
903 replicates.

904 ***Immunoprecipitation of ORPs***

905 HeLa cells transfected with EGFP-tagged ORPs were washed in cold PBS and lysed
906 on ice in lysis buffer [50 mM Tris, 120 mM NaCl, 40 mM Hepes, 0,5% digitonin, 0,5%
907 CHAPS, pH 7.36, and protease inhibitor cocktail (Roche). Cell lysates were then
908 centrifuged at 21 000 g for 20 min at 4°C. Supernatants were then incubated with
909 Chromotek GFP-trap agarose beads (Allele Biotech) for 1 hour at 4°C under rotation.
910 Subsequently beads were washed in 0.1 M phosphate buffer. After extensive washes
911 in cold lysis buffer, immunoprecipitated proteins bound to the beads were processed

912 for Mass Spectrometry analysis (see below) or incubated in sample buffer (containing
913 2% SDS) and then boiled for 1 min. In the latter case immunoprecipitates were
914 loaded and separated in 10% SDS–PAGE gel and immunoblotting was carried out.

915 ***Cell fractionation***

916 HeLa cells (100x10^6 cells) were harvested 48 hours after transfection with siRNA
917 oligos and washed with PBS by centrifugation at 600 g for 5 min. The cell pellet was
918 resuspended in starting buffer (225 mM mannitol, 75 mM sucrose and 30 mM Tris-
919 HCl pH 7.4) and homogenized using a Tissue Grinder Dura-Grind®, Stainless Steel,
920 Dounce (Wheaton). The homogenate was centrifuged three times at 600 g for 5 min
921 to remove nuclei and unbroken cells. The crude mitochondria was pelleted by
922 centrifugation at 10 000 g for 10 min. To separate MAM and pure mitochondria
923 fractions, the pellet was resuspended in MRB buffer (250 mM mannitol, 5 mM
924 HEPES and 0.5 mM EGTA, pH 7.4) and layered on top of different concentrations of
925 Percoll gradient (225 mM mannitol, 25 mM HEPES, 1 mM EGTA pH 7.4 and 30% or
926 15% Percoll). After centrifugation at 95 000 g for 30 min, two dense bands containing
927 either the pure mitochondria or MAM fraction were recovered and washed twice with
928 MRB buffer by centrifugation at 6300 g for 10 min to remove residual Percoll and
929 residual contamination. MAM was pelleted by centrifugation at 100 000 g for 1 hour.
930 MAMs and pure mitochondria pellets were resuspended in Lysis Buffer (50 mM Tris,
931 150 mM NaCl, 1% Triton X-100, 10 mM EDTA, pH 7.2, and protease inhibitor
932 cocktail) and protein concentrations were determined by Bradford assay. Equal
933 amount of proteins were loaded on 4-20% gradient SDS-PAGE gels (Biorad) and
934 immunoblotting was carried out. Pure mitochondria were processed for MS-lipidomic
935 analysis (see below).

936 ***Mass spectrometry-proteomic analysis***

937 Mass Spectrometry (MS) analysis was carried out by the proteomics/mass
938 spectrometry platform in IJM (http://www.ijm.fr/plateformes/spectrometrie-de-masse).
939 Briefly, after washes with binding buffer, immunoprecipitations beads were rinsed
940 with 100 µl of NH4HCO3 25 mmol/l. Proteins on beads were digested overnight at
941 37°C by sequencing grade trypsin (12,5 µg/ml; Promega Madison, Wi, USA) in 20 µl
942 of NH4HCO3 25 mmol/l. Digests were analysed by an Orbitrap Fusion (Thermo
943 Fisher Scientific, San Jose, CA) equipped with a Thermo Scientific EASY-Spray
944 nanoelectrospray ion source and coupled to an Easy nano-LC Proxeon 1000 system
945 (Thermo Fisher Scientific, San Jose, CA). MS/MS data were processed with
946 Proteome Discoverer 1.4 software (Thermo Fisher scientific, San Jose, CA) coupled
947 to an in house Mascot search server (Matrix Science, Boston, MA ; version 2.4.2).
948 MS/MS datas were searched against SwissProt databases with Homo sapiens
949 taxonomy.
950
951 **Mass Spectrometry-lipidomic analysis**
952 700 µl of homogenized cells were mixed with 800 µl 1 N HCl:CH_3OH 1:8 (v/v), 900 µl
953 $CHCl_3$ and 200 µg/ml of the antioxidant 2,6-di-tert-butyl-4-methylphenol (BHT; Sigma
954 Aldrich). The organic fraction was evaporated using a Savant Speedvac spd111v
955 (Thermo Fisher Scientific). Lipid pellets were reconstituted in running solution
956 (CH_3OH:$CHCl_3$:NH_4OH; 90:10:1.25; v/v/v). Phospholipid species were analyzed by
957 electrospray ionization tandem mass spectrometry (ESI-MS/MS) on a hybrid triple
958 quadrupole/linear ion trap mass spectrometer (4000 QTRAP system; Applied
959 Biosystems SCIEX) equipped with a TriVersa NanoMate (Advion Biosciences)
960 robotic nanosource. Phospholipid profiling was executed by (positive or negative)
961 precursor ion or neutral loss scanning at a collision energy of 35 eV for neutral loss

962 141 (phosphatidylethanolamine (PE)). Phospholipid quantification was performed by
963 multiple reaction monitoring (MRM), the transitions being based on the neutral losses
964 or the typical product ions as described above. The MRM dwell time was set to 100
965 ms and typically the signal was averaged over 20 cycles. Lipid standards used were
966 PE25:0 and PE43:6 (Avanti Polar Lipids). The data were corrected for isotope effects
967 as described by (Liebisch, Lieser et al., 2004).
968

969 **Lipid Transfer assay**

970 ***ORP5 and ORP8 ORD domain purification***

971 Escherichia coli BL21DE3 RILP (Invitrogen) cells were transformed with plasmids
972 encoding for GST tagged ORP5 or ORP8 ORD domains following the manufacturer's
973 instruction. Bacteria were then grown overnight at 37°C and used to inoculate a
974 large-scale volume (1L). When the OD_{600} reached 0.4, cultures were cool down and
975 incubate at 18°C until they reached O_{D600} = 0.65. Cells were induced by addition
976 of isopropyl β-D-1-thiogalactopyranoside to a final concentration of 0.1 mM and were
977 incubated overnight at 18°C before harvesting. Cells were resuspended in 35 ml
978 binding buffer (1X PBS, 1 mM EDTA, 1 mM DTT, Protease inhibitor) then 250 units
979 of benzonase nuclease (Sigma) were added to the resuspension. Cells were lysed by
980 sonication and the supernatant was recover after 20 min centrifugation at 184 000g
981 and 4°C. Supernatant containing GST tagged proteins was incubated with 2 ml of
982 Glutathione Sepharose 4 fast flow for 1 hour at 4°C under nutation. Beads were
983 washed using a serie of wash buffer: 1st (1X PBS, 1 mM EDTA, 1 mM DTT), 2nd HSP-
984 removal buffer (50 mM Tris pH7.5, 50 mM KCl, 20 mM MgCl2, 5 mM ATP) then
985 cleavage buffer (50 mM Tris pH 7.5, 150 mM NaCl, 1 mM EDTA, 1 mM DTT).
986 Cleavage of the GST tag was realized overnight at 4°C using Prescission protease.

987 Untagged proteins were eluted with cleavage buffer, flash frozen and stored at -80°C
988 until lipid transfer assay was performed.

989 ***Lipids***

990 1-palmitoyl-2-oleoyl-sn-glycero-3-phosphocholine (POPC), 1,2-dioleoyl-sn-glycero-3-
991 phosphoethanolamine-N-(cap biotinyl) (Biotinyl Cap PE), 1-palmitoyl-2-
992 (dipyrrometheneboron difluoride)undecanoyl-sn-glycero-3-phosphoethanolamine
993 (TopFluor-PE), 1-palmitoyl-2-(dipyrrometheneboron difluoride)undecanoyl-sn-
994 glycero-3-phospho-L-serine (TopFluor-PS), 1-palmitoyl-2-(dipyrrometheneboron
995 difluoride)undecanoyl-sn-glycero-3-phosphocholine (TopFluor-PC) were purchased
996 from Avanti Polar Lipids as chloroform solutions.

997 ***Liposome preparation***

998 1 µmol of the appropriate lipid mixtures in chloroform solution was dried in glass
999 tubes for 10 min under a gentle stream of argon, and then for 1 hour under vacuum.
1000 The dried lipid films were resuspended in 1 ml of buffer H (25 mM HEPES/KOH, pH
1001 7.7; 150 mM KCL; 10% Glycerol) by vigorously vortexing for 30 min at room
1002 temperature. Unilamellar liposomes were produced by seven freeze-thaw cycles (30
1003 sec in liquid nitrogen followed by 5 min in a 37°C water bath) and extrusion (at least
1004 21 times) through a polycarbonate filter with 100 nm pore size (polycarbonate
1005 membranes from Avanti Polar Lipids). The liposomes were then stored on ice.

1006 ***Lipid Transfer assay in vitro***

1007 The lipid transfer assays were realized with liposomes prepared as described above.
1008 The donor liposomes contained 1% mol TopFluor lipids (-PS, -PC or -PE) and 2%
1009 mol of Biotinyl Cap PE. The acceptor liposomes contained only POPC. For each
1010 reaction, 25µL of streptavidin-coated magnetic beads (DynabeadsMyOne
1011 Streptavidin T1, Invitrogen) were washed in buffer H and mixed with 25µL of 1 mM

1012 donor liposomes. The mixture was incubated for 1 hour at 25°C with intermittent
1013 gentle mixing. Bead-bound donor liposomes were then washed, resuspended in
1014 25µL and mixed with 25µL of 1 mM acceptor liposomes and 50µL of buffer H or
1015 protein (0.3 µM protein and 2.5 µM TopFluor lipids in the reaction solution). The
1016 mixture was incubated at 37°C for 1 hour with intermittent gentle mixing. Supernatant
1017 containing acceptor liposomes was recovered after binding of bead-bound donor
1018 liposomes to a magnetic rack. TopFluor fluorescence of acceptor and donor
1019 liposomes was measured (after solubilization with 0.4% (w/v) n-dodecyl-β-D-
1020 maltoside, DDM) in a SpectraMax M5 plate reader (Molecular Device) equilibrated to
1021 30°C (excitation: 450 nm; emission: 510 nm; cutoff: 475 nm; low gain). The
1022 percentage of lipids transferred from donor to acceptor liposomes was determined
1023 using the following formula: $100*F_{acceptor}/(F_{acceptor}+F_{donor})$. To confirm that
1024 fluorescence was transferred to acceptor liposomes, a fraction of the reaction
1025 supernatant – which has not been solubilized with DDM – was floated on a Nycodenz
1026 density gradient. 50 µL of supernatant was mixed with 100 µL of buffer H and 150 µL
1027 of Nycodenz 80% in buffer H. The solution was transferred to a 0.8 mL Ultra-Clear
1028 centrifuge tube (Beckman Coulter) and overlaid with 250 µL of Nycodenz 30% in
1029 buffer H and 75 µL of buffer H. The tubes were centrifuged in a SW 55 Ti rotor
1030 (Beckman Coulter) at 246,000 g for 4 hours at 4 °C. 50 µL were collected from the
1031 top of the gradient and the fluorescence was measured.
1032
1033 **Radiometric assay for the conversion of PS to PE**
1034 Hela cells were seeded on 6-well plates and transfected for 48 hours with the non-
1035 targeting, ORP5 or ORP8-specific siRNAs specified above by using Oligofectamine
1036 (Thermo Fisher Scientific). The cells were then washed and shifted into Hanks

1037 balanced salt solution (Gibco) supplemented with a serine-free MEM amino acid
1038 mixture and MEM vitamins (Gibco), followed by 18 hours labeling with 2 μl/well L-
1039 [^{3}H(G)]serine (30.9 Ci/mmol, NET24800, Perkin-Elmer)(Fig. 1e). In parallel
1040 experiments (Fig. 1f) cells were starved in serum-free medium for 10 hours and then
1041 treated with 1mM β-chloro-L-alanine (SIGMA) for 2 hours or left in serum-free
1042 medium, followed by 1hr pulse with 15 μCi/ml of [^{3}H(G)]serine and 12 hours chase in
1043 serum-free DMEM. After the labeling (Fig. 1e) or the chase (Fig. 1f), the cells were
1044 scraped into 0.9 ml 2% NaCl per well, a 0.1 ml aliquot was withdrawn for protein
1045 analysis with the BCA assay (Thermo Fisher Scientific), and, after adding 50 nmol of
1046 unlabeled PS as carrier, the remaining 0.8 ml was subjected to lipid extraction by an
1047 acid modification of the Folch method (Kim, Song et al., 2017). After drying, the lipids
1048 were resolved in 50 μl $CHCl_3$ and applied on Merck TLC Silica gel 60^{TM} plates,
1049 followed by separation by using $CHCl_3$-methanol-acetic acid-H2O (50:30:8:3.5) as
1050 solvent. The PS and PE spots identified from the mobility of standards run on the
1051 same plates were scraped into scintillation vials for analysis of [^{3}H] radioactivity. The
1052 DPM values were corrected for total cell protein, and the ratio of [^{3}H] in PE vs. PS
1053 calculated.
1054
1055 **Mitochondrial respiration assay**
1056 Oxygen Consumption rate (OCR) was measured using the XF_p Extracellular Flux
1057 Analyzer (Seahorse Bioscience Inc.). HeLa cells were seeded on a 6-well plate 3
1058 days before the Seahorse experiment and knockdown of the proteins of interest was
1059 realized 2 days before. The day after the knockdown, HeLa cells transfected with
1060 Ctrl, ORP5, ORP8 or ORP5 and ORP8 siRNAs were plated in a Seahorse XFp 8-
1061 mini wells microplate. 20,000 HeLa cells were seeded in each well (except in the

1062 blank wells used for the background correction) in 180 μl of culture medium, and
1063 incubated overnight at 37℃ in 5% CO2. One day after, the culture medium was
1064 replaced with 180 µl of XF DMEM Medium Solution pH 7.4 and then the 8-mini wells
1065 microplate was moved in a 37°C non-CO2 incubator before measurement. OCR was
1066 determined before drug additions and after addition of Oligomycin (1.5 µM), Carbonyl
1067 cyanide 4-(trifluoromethoxy) phenylhydrazone (FCCP, 0.5 µM), and
1068 Rotenone/Antimycin A (0.5 µM) (purchased from Agilent). After each assay, all the
1069 raw OCR data were analyzed using WAVE software.
1070
1071 **Fluorescence Microscopy**
1072 ***Immunofluorescence and Confocal Microscopy***
1073 HeLa cells were seeded on 13 mm glass bottom coverslips (Agar Scientific).
1074 Immunofluorescence was carried out one day after transfection. Transfected cells
1075 were fixed with 4% PFA/PBS for 15 min at room temperature, washed in PBS and
1076 incubated with 50 mM NH4Cl/PBS for 15 min at room temperature. After washing
1077 with PBS and blocking buffer (1% BSA/ 0,1% Saponin in PBS), cells were incubated
1078 with primary antibodies diluted in blocking buffer for 1 hour at room temperature and
1079 then with fluorescently-labeled secondary antibodies. After washing with blocking
1080 buffer and then PBS, coverslips were mounted on microscopy slides and images
1081 were acquired on Confocal inverted microscope SP8-X (DMI 6000 Leica). Optical
1082 sections were acquired with a 63x/1.4 Oil immersion objective using the LAS-X
1083 software and fluorescent pictures were collected with a PMTs GaAsP hybride camera
1084 (Hamamatsu). Images from a mid-focal plane are shown. Images were processed
1085 and fluorescence was analysed off line using Image J.
1086
1087 **Calcium (Ca^{2+}) indicators**

1088 ***Ca^{2+} intake assay using Geco constructs***

1089 HeLa cells were seeded on glass bottom ibidi chambers (µ-slide 2 wells) 3 days
1090 before imaging. Knockdown of the proteins of interest was realized 2 days before
1091 imaging, as described above. The day after knockdown, 0.8 µg of GECO plasmid
1092 were transfected with 6 µl of lipofectamine 2000/well (Invitrogen), according to the
1093 manufacturer's instructions. The day of imaging, cells were washed 4-5 hours before
1094 the imaging with fresh DMEM. Cell imaging was performed on an inverted Nikon Ti
1095 Eclipse E microscope coupled with a Spinning Disk (Yokogawa CSU-X1-A1) and
1096 cage incubator to control both temperature and CO_2 (37 °C, 5% CO2). After
1097 excitation with a 561 nm laser (Coherent, 100 mW), fluorescence from GECO
1098 constructs was detected with a 40X oil immersion objective (PLAN FLUOR; NA: 1.30;
1099 Nikon) and a Prime 95B sCMOS camera (Photometrics). Images were captured
1100 every 5 sec during 10 min. Approximatively 1 min after the start of captures,
1101 histamine was added to a final concentration of 100 µM to trigger Ca^{2+} release from
1102 intracellular stores. Image analysis was performed using Image J by measuring the
1103 fluorescence intensity over time (time-lapse) of cells expressing the GECO
1104 constructs. Histograms represent the response of the cell to the addition of histamine
1105 shown as the maximum fluorescence (Fmax) after treatment / mean fluorescence
1106 before histamine F0.

1107 ***Ratiometric Ca^{2+} imaging using a mt-Pericam construct***

1108 HeLa cells were seeded on glass bottom ibidi chambers (µ-slide 2 wells) 3 days
1109 before imaging. Knockdown of the proteins of interest was realized 2 days before
1110 imaging, as described above. The day after knockdown, 2.4 µg of mt-Pericam
1111 plasmid were transfected with 6 µl of lipofectamine 2000/well (Invitrogen), according

1112 to the manufacturer's instructions. The day of imaging, cells were washed 4-5 hours
1113 before the imaging with fresh DMEM.
1114 Imaging of mt-pericam was performed on an inverted Nikon Ti Eclipse Eclipse-E
1115 microscope coupled with a Spinning Disk (Yokogawa, CSU-X1-A1), a 40x CFI Plan
1116 Fluor objective (Nikon, NA 1.30, oil immersion) and a sCMOS camera (Photometrics,
1117 Prime 95B) with a binning of 2. Knock-down cells expressing pericam constructs
1118 were imaged in a controlled atmosphere (37°C, 5% CO_2). For each field of view, a
1119 time-lapse was recorded with an image every 8 sec during 10 min. Approximatively 3
1120 min after the start of captures, histamine was added to a final concentration of 100
1121 µM. For each time point mt-pericam fluorescence was collected using a 525/45
1122 bandpass filter (Semrock) after alternative excitation at 405 nm (Vortran, 100mW
1123 laser) and 488 nm (Vortran, 150mW laser). A perfect focus system (Nikon) was used
1124 to keep the focus constant along the timelapse, the whole system was driven by
1125 Metamorph (version 7.7, Molecular Devices).
1126 All the image processing and quantification was performed using a custom script in
1127 Image J. First, images were corrected for flat-field and dark noise using reference
1128 images respectively acquired on a fluorescent plastic slide (Chroma) and with no light
1129 reaching the detector. Regions of interest were also drawn on an empty area of every
1130 stack to perform a background subtraction on every image. Then hyperstacks
1131 containing two channels were registered to correct any lateral drift of the sample
1132 during the acquisition using the Image J plugin "HyperStackReg (v05)" with the
1133 "translation" algorithm. Once the stacks were processed, regions of interest were
1134 drawn around individual cells, a threshold applied (Mean) and the mean intensity of
1135 each cell recorded on each image pair along the time-lapse. For every cell the ratio
1136 488/405 was plotted along the time and only the cells with a stable ratio during the

1137 first 3 min time points and with a sharp increase observed after addition of histamine
1138 were kept for the final analysis.
1139
1140 **Flow cytometry for TMRE analysis**
1141 ***Membrane potential studies using TMRE- Mitochondrial Membrane Potential***
1142 ***Assay Kit***
1143 HeLa cells were seeded on 6-well plates 3 days before TMRE detection and the day
1144 after they were transfected for 48 hours with the non-targeting, ORP5 or ORP8-
1145 specific siRNAs specified above. The day before analysis, the medium was replaced
1146 with DMEM 10% FBS with or without 20 µM CCCP (Carbonyl cyanide m-
1147 chlorophenyl hydrazine) at 37°C and 5% CO_2 to induce mitochondrial depolarization.
1148 After 24 hours, 200 nM of TMRE in DMEM 10% FBS (Mitochondrial Membrane
1149 Potential Assay Kit, abcam ab113852) was added to cells and replaced after 30 min.
1150 Cells were kept at 37°C and 5% CO_2 for additional 15 min and then trypsinized and
1151 resuspended in DMEM (1-2x105 cells in 500 µl). TMRE was then analysed by flow
1152 cytometry.
1153 ***Flow cytometry***
1154 Multicolor flow cytometry was conducted on Beckman Coulter's CytoFLEX S
1155 cytometer. Analyses were performed using Beckman Coulter's Kaluza and CytExpert
1156 software. TMRE (Ex/Em = 549/575) was excited by a 561 nm laser and detected
1157 through a 585/542 nm filter channel. All acquisitions were made on 10 000 cells. All
1158 data are presented as mean ±SEM of three independent experimental replicates.
1159
1160 **Apoptosis assay using Cleaved-caspase-3 expression**

1161 HeLa cells were seeded on glass bottom 13 mm coverslips in a 24 well plates. The
1162 next day, 48 hours knockdown of the proteins of interest were realized as described
1163 above. 2 days after the knockdown, cells were treated with 1 µM staurosporine or
1164 with DMSO to induce apoptosis. After 4 hours apoptotic cells were analyzed by
1165 confocal immunofluorescence, using cleaved Caspase-3 antibody and Mitotracker
1166 red to label mitochondria. Cleaved Caspase-3 positive cells were quantified using the
1167 Cell Counter plugin from Image J Software. All data are presented as mean ±SEM of
1168 three experimental replicates.
1169

1170 **Senescence studies using SA-β-Galactosidase assay and crystal violet**
1171 **staining**

1172 For SA-β-galactosidase assay, cells were washed twice with PBS and fixed 5 min
1173 with 2% formaldehyde / 0.2% glutaraldehyde. Cells were then rinsed twice in PBS
1174 and incubated at 37°C overnight in SA-β-Gal staining solution as previously
1175 described (Itahana, Campisi et al., 2007).
1176 For crystal violet staining, cells were washed with PBS, fixed for 15 min in 3.7%
1177 formaldehyde and then stained with 0.5% crystal violet solution. After drying, plates
1178 were scanned.
1179 Relative cell count was determined by dissolving crystal violet in acetic acid solution
1180 and measuring optical density at 595 nM.
1181

1182 **Electron Microscopy Analysis**

1183 ***Conventional EM***

1184 For conventional EM, cells grown on 13 mm glass bottom coverslips (Agar Scientific)
1185 were fixed with 2.5% glutaraldehyde and 2% PFA in 0.1 M cacodylate, 0.05% $CaCl_2$

1186 buffer for 24 hours. After several washes with 0.1 M cacodylate buffer, the cells were
1187 postfixed with 1% OsO_4, 1.5% potassium ferricyanide in 0.1M Cacodylate for 1 hour.
1188 After several washes with 0.1 M cacodylate buffer and H_2O, the cells were stained
1189 with 0.5% uranyl acetate for 24 hours. After several washes with H_2O, the cells were
1190 dehydrated in ethanol and embedded in Epon while on the coverslips. Ultrathin
1191 sections were prepared, counterstained with uranyl acetate and observed under a
1192 MET JEOL 1400 equipped with a Orius High speed (Gatan) camera.

1193 ***HRP Detection***

1194 HeLa cells expressing HRP-KDEL were fixed on coverslips with 1.3% glutaraldehyde
1195 in 0.1 M cacodylate buffer, washed in 0.1 M ammonium phosphate [pH 7.4] buffer for
1196 1 hour and HRP was visualized with 0.5 mg/ml DAB and 0.005% H_2O_2 in 0.1 M
1197 Ammonium Phosphate [pH 7.4] buffer. Development of HRP (DAB dark reaction
1198 product) took between 5 min to 20 min and was stopped by extensive washes with
1199 cold water. Cells were postfixed in 2% OsO_4+1% $K_3Fe(CN)_6$ in 0.1 M cacodylate
1200 buffer at 4°C for 1 hour, washed in cold water and then contrasted in 0.5% uranyl
1201 acetate for 2 hours at 4°C, dehydrated in an ethanol series and embedded in epon as
1202 for conventional EM. Ultrathin sections were counterstained with 2% uranyl acetate
1203 and observed under a FEI Tecnai 12 microscope equipped with a CCD (SiS 1kx1k
1204 keenView) camera.

1205 ***Immunogold labelling***

1206 HeLa cells were fixed with a mixture of 2%PFA and 0.125% glutaraldehyde in 0.1 M
1207 phosphate buffer [pH 7.4] for 2 hours, and processed for ultracryomicrotomy as
1208 described previously (Slot & Geuze, 2007). Ultrathin cryosections were single- or
1209 double-immunogold-labeled with antibodies and protein A coupled to 10 or 15 nm
1210 gold (CMC, UMC Utrecht, The Netherlands), as indicated in the legends to the

1211 figures. Immunogold-labeled cryosections were observed under a FEI Tecnai 12
1212 microscope equipped with a CCD (SiS 1kx1k keenView) camera.

1213 ***Quantifications***

1214 For the quantification of the number of cristae junction in Epon sections, about 200
1215 mitochondria were analyzed in randomly selected cell profiles and cristae junctions
1216 were counted in each of the mitochondria profile and reported as number of
1217 cristae/mitochondria profile. All data are presented as mean ±SEM of three
1218 experimental replicates.

1219 For the quantification of ER-mitochondria contact sites in HRP-stained Epon
1220 sections, the total circumference of each mitochondria and the length of the multiple
1221 HRP-positive ER segments closely associated (<30 nm) with them were measured
1222 by iTEM software (Olympus) on acquired micrographs of HeLa cells for each of 20-
1223 30 cell profiles, as indicated in the figure legends. Cells were randomly selected for
1224 analysis without prior knowledge of transfected plasmid or siRNA. All data are
1225 presented as mean (%) ±SEM of three experimental replicates.

1226 For the quantification of immunogold labeling on ultrathin cryosections, 150 gold
1227 particles were counted on acquired micrographs of randomly selected cell profiles at
1228 specific ranges of distance from CJ (0-50, 50-100, 100-150, 150-200 nm) in each of
1229 three experiments. All data are presented as mean (%) ±SEM of three experimental
1230 replicates.

1231 **ACKNOWLEDGEMENTS**

1232 We thank Dr V. Kozjak-Pavlovic, P. Pinton and P. Somerharju for kindly sharing
1233 reagents and advices with us. We also thank Dr. R. Legouis for discussion; Claire
1234 Boulogne, Mickael Bourge, and Remi Le Borgne for help and consultation with
1235 microscopy experiments and flow cytometry; Naima El Khallouki, Blandine

Bourigault, Riikka Kosonen and Liisa Arala for technical assistance. The present work has benefited from Imagerie-Gif core facility supported by l' Agence Nationale de la Recherche (ANR-11-EQPX-0029/Morphoscope, ANR-10-INBS-04/FranceBioImaging; ANR-11-IDEX-0003-02/ Saclay Plant Sciences). For the Immuno-EM and HRP-KDEL EM analysis/quantifications we acknowledge the ImagoSeine facility, member of the France BioImaging infrastructure supported by grant ANR-10-INBS-04 from the French National Research Agency. We also thank Jean-Michel Camadro and Thibault Leger (IJM proteomics platform) for proteomics analysis. This work was supported by ANR Jeune Chercheur (ANR0015TD and ATIP-Avenir Program to F.G.; the Academy of Finland (grants 285223 and 322647), the Sigrid Juselius Foundation, the Finnish Foundation for Cardiovascular Research and the Magnus Ehrnrooth Foundation to V.M.O.; the Fondation ARC pour la recherche sur le cancer and INCA (N°2018-144) to D.B.; the "Association Française contre les Myopathies" (AFM Research grant 20123) and the ITMO-Inserm Plan Cancer 2014-2019 to D.T.

AUTHOR CONTRIBUTIONS

FG conceived and supervised the work. VO designed and supervised the radiometric assays for PS-to-PE conversion and the expression analysis by RT-PCR. DT designed and supervised the *in vitro* lipid transfer assays. DB designed and supervised the senescence assays including part of the RT-PCR analysis. LR and CS performed and analyzed the cell experiments including Ca^{2+} imaging. LR, AH, and FG performed and analyzed the EM experiments. CS, AH and DT performed and analyzed the *in vitro* lipid transfer assays. EJ, AA and AK performed and

1261 analyzed the radiometric assays for PS-to-PE conversion. EM, JD and JS performed
1262 MS-lipidomic analysis. RLB provided tools and techniques for Ca^{2+} imaging analysis.
1263 JN provided technical help and generated some of the constructs for mammalian cell
1264 expression. XM performed the senescence experiments. LR, CS and FG wrote the
1265 manuscript and all authors commented on the manuscript.
1266

1267 **DECLARATION OF INTERESTS**

1268 The authors declare that they have no competing interests.
1269
1270
1271

1272 **REFERENCES**

1273 Aaltonen MJ, Friedman JR, Osman C, Salin B, di Rago JP, Nunnari J, Langer T, Tatsuta T
1274 (2016) MICOS and phospholipid transfer by Ups2-Mdm35 organize membrane lipid
1275 synthesis in mitochondria. The Journal of cell biology 213: 525-34
1276 Bottinger L, Horvath SE, Kleinschroth T, Hunte C, Daum G, Pfanner N, Becker T (2012)
1277 Phosphatidylethanolamine and cardiolipin differentially affect the stability of
1278 mitochondrial respiratory chain supercomplexes. Journal of molecular biology 423: 677-
1279 86
1280 Chen H, Born E, Mathur SN, Field FJ (1993) Cholesterol and sphingomyelin syntheses are
1281 regulated independently in cultured human intestinal cells, CaCo-2: role of membrane
1282 cholesterol and sphingomyelin content. J Lipid Res 34: 2159-67
1283 Chung J, Torta F, Masai K, Lucast L, Czapla H, Tanner LB, Narayanaswamy P, Wenk MR,
1284 Nakatsu F, De Camilli P (2015) INTRACELLULAR TRANSPORT. PI4P/phosphatidylserine
1285 countertransport at ORP5- and ORP8-mediated ER-plasma membrane contacts. Science
1286 349: 428-32
1287 Colombini M (2012) VDAC structure, selectivity, and dynamics. Biochimica et biophysica
1288 acta 1818: 1457-65
1289 De Stefani D, Bononi A, Romagnoli A, Messina A, De Pinto V, Pinton P, Rizzuto R (2012)
1290 VDAC1 selectively transfers apoptotic Ca2+ signals to mitochondria. Cell Death Differ 19:
1291 267-73
1292 Ding C, Wu Z, Huang L, Wang Y, Xue J, Chen S, Deng Z, Wang L, Song Z, Chen S (2015)
1293 Mitofilin and CHCHD6 physically interact with Sam50 to sustain cristae structure. Sci
1294 Rep 5: 16064
1295 Du X, Turner N, Yang H (2017) The role of oxysterol-binding protein and its related
1296 proteins in cancer. Semin Cell Dev Biol
1297 Du X, Zadoorian A, Lukmantara IE, Qi Y, Brown AJ, Yang H (2018) Oxysterol-binding
1298 protein-related protein 5 (ORP5) promotes cell proliferation by activation of mTORC1
1299 signaling. The Journal of biological chemistry 293: 3806-3818

1300 Filippin L, Abad MC, Gastaldello S, Magalhaes PJ, Sandona D, Pozzan T (2005) Improved
1301 strategies for the delivery of GFP-based Ca2+ sensors into the mitochondrial matrix. Cell
1302 calcium 37: 129-36
1303 Friedman JR, Mourier A, Yamada J, McCaffery JM, Nunnari J (2015) MICOS coordinates
1304 with respiratory complexes and lipids to establish mitochondrial inner membrane
1305 architecture. eLife 4
1306 Galmes R, Houcine A, van Vliet AR, Agostinis P, Jackson CL, Giordano F (2016)
1307 ORP5/ORP8 localize to endoplasmic reticulum-mitochondria contacts and are involved
1308 in mitochondrial function. EMBO reports 17: 800-10
1309 Ghai R, Du X, Wang H, Dong J, Ferguson C, Brown AJ, Parton RG, Wu JW, Yang H (2017)
1310 ORP5 and ORP8 bind phosphatidylinositol-4, 5-biphosphate (PtdIns(4,5)P 2) and
1311 regulate its level at the plasma membrane. Nature communications 8: 757
1312 Giordano F (2018) Non-vesicular lipid trafficking at the endoplasmic reticulum-
1313 mitochondria interface. Biochemical Society transactions 46: 437-452
1314 Guarani V, McNeill EM, Paulo JA, Huttlin EL, Frohlich F, Gygi SP, Van Vactor D, Harper JW
1315 (2015) QIL1 is a novel mitochondrial protein required for MICOS complex stability and
1316 cristae morphology. eLife 4
1317 Hanada K, Nishijima M, Kiso M, Hasegawa A, Fujita S, Ogawa T, Akamatsu Y (1992)
1318 Sphingolipids are essential for the growth of Chinese hamster ovary cells. Restoration of
1319 the growth of a mutant defective in sphingoid base biosynthesis by exogenous
1320 sphingolipids. The Journal of biological chemistry 267: 23527-33
1321 Harner M, Korner C, Walther D, Mokranjac D, Kaesmacher J, Welsch U, Griffith J, Mann M,
1322 Reggiori F, Neupert W (2011) The mitochondrial contact site complex, a determinant of
1323 mitochondrial architecture. The EMBO journal 30: 4356-70
1324 Heikinheimo L, Somerharju P (1998) Preferential decarboxylation of hydrophilic
1325 phosphatidylserine species in cultured cells. Implications on the mechanism of transport
1326 to mitochondria and cellular aminophospholipid species compositions. The Journal of
1327 biological chemistry 273: 3327-35
1328 Herrera-Cruz MS, Simmen T (2017) Of yeast, mice and men: MAMs come in two flavors.
1329 Biol Direct 12: 3
1330 Hirabayashi Y, Kwon SK, Paek H, Pernice WM, Paul MA, Lee J, Erfani P, Raczkowski A,
1331 Petrey DS, Pon LA, Polleux F (2017) ER-mitochondria tethering by PDZD8 regulates
1332 Ca(2+) dynamics in mammalian neurons. Science 358: 623-630
1333 Hohr AIC, Lindau C, Wirth C, Qiu J, Stroud DA, Kutik S, Guiard B, Hunte C, Becker T,
1334 Pfanner N, Wiedemann N (2018) Membrane protein insertion through a mitochondrial
1335 beta-barrel gate. Science 359
1336 Huynen MA, Muhlmeister M, Gotthardt K, Guerrero-Castillo S, Brandt U (2016) Evolution
1337 and structural organization of the mitochondrial contact site (MICOS) complex and the
1338 mitochondrial intermembrane space bridging (MIB) complex. Biochimica et biophysica
1339 acta 1863: 91-101
1340 Itahana K, Campisi J, Dimri GP (2007) Methods to detect biomarkers of cellular
1341 senescence: the senescence-associated beta-galactosidase assay. Methods Mol Biol 371:
1342 21-31
1343 John GB, Shang Y, Li L, Renken C, Mannella CA, Selker JM, Rangell L, Bennett MJ, Zha J
1344 (2005) The mitochondrial inner membrane protein mitofilin controls cristae
1345 morphology. Molecular biology of the cell 16: 1543-54
1346 Joshi AS, Thompson MN, Fei N, Huttemann M, Greenberg ML (2012) Cardiolipin and
1347 mitochondrial phosphatidylethanolamine have overlapping functions in mitochondrial
1348 fusion in Saccharomyces cerevisiae. The Journal of biological chemistry 287: 17589-97

1349 Kim SH, Song HE, Kim SJ, Woo DC, Chang S, Choi WG, Kim MJ, Back SH, Yoo HJ (2017)
1350 Quantitative structural characterization of phosphatidylinositol phosphates from
1351 biological samples. J Lipid Res 58: 469-478
1352 Kopec KO, Alva V, Lupas AN (2010) Homology of SMP domains to the TULIP superfamily
1353 of lipid-binding proteins provides a structural basis for lipid exchange between ER and
1354 mitochondria. Bioinformatics 26: 1927-31
1355 Kornmann B, Currie E, Collins SR, Schuldiner M, Nunnari J, Weissman JS, Walter P (2009)
1356 An ER-mitochondria tethering complex revealed by a synthetic biology screen. Science
1357 325: 477-81
1358 Kozjak V, Wiedemann N, Milenkovic D, Lohaus C, Meyer HE, Guiard B, Meisinger C,
1359 Pfanner N (2003) An essential role of Sam50 in the protein sorting and assembly
1360 machinery of the mitochondrial outer membrane. The Journal of biological chemistry
1361 278: 48520-3
1362 Kozjak-Pavlovic V, Ross K, Benlasfer N, Kimmig S, Karlas A, Rudel T (2007) Conserved
1363 roles of Sam50 and metaxins in VDAC biogenesis. EMBO reports 8: 576-82
1364 Kumar N, Leonzino M, Hancock-Cerutti W, Horenkamp FA, Li P, Lees JA, Wheeler H,
1365 Reinisch KM, De Camilli P (2018) VPS13A and VPS13C are lipid transport proteins
1366 differentially localized at ER contact sites. The Journal of cell biology 217: 3625-3639
1367 Lang A, John Peter AT, Kornmann B (2015) ER-mitochondria contact sites in yeast:
1368 beyond the myths of ERMES. Current opinion in cell biology 35: 7-12
1369 Liebisch G, Lieser B, Rathenberg J, Drobnik W, Schmitz G (2004) High-throughput
1370 quantification of phosphatidylcholine and sphingomyelin by electrospray ionization
1371 tandem mass spectrometry coupled with isotope correction algorithm. Biochimica et
1372 biophysica acta 1686: 108-17
1373 Ma X, Warnier M, Raynard C, Ferrand M, Kirsh O, Defossez PA, Martin N, Bernard D
1374 (2018) The nuclear receptor RXRA controls cellular senescence by regulating calcium
1375 signaling. Aging Cell 17: e12831
1376 Maeda K, Anand K, Chiapparino A, Kumar A, Poletto M, Kaksonen M, Gavin AC (2013)
1377 Interactome map uncovers phosphatidylserine transport by oxysterol-binding proteins.
1378 Nature 501: 257-61
1379 Martin N, Bernard D (2018) Calcium signaling and cellular senescence. Cell calcium 70:
1380 16-23
1381 Moser von Filseck J, Copic A, Delfosse V, Vanni S, Jackson CL, Bourguet W, Drin G (2015)
1382 INTRACELLULAR TRANSPORT. Phosphatidylserine transport by ORP/Osh proteins is
1383 driven by phosphatidylinositol 4-phosphate. Science 349: 432-6
1384 Nagai T, Sawano A, Park ES, Miyawaki A (2001) Circularly permuted green fluorescent
1385 proteins engineered to sense Ca2+. Proceedings of the National Academy of Sciences of
1386 the United States of America 98: 3197-202
1387 Ott C, Dorsch E, Fraunholz M, Straub S, Kozjak-Pavlovic V (2015) Detailed analysis of the
1388 human mitochondrial contact site complex indicate a hierarchy of subunits. PloS one 10:
1389 e0120213
1390 Patron M, Raffaello A, Granatiero V, Tosatto A, Merli G, De Stefani D, Wright L,
1391 Pallafacchina G, Terrin A, Mammucari C, Rizzuto R (2013) The mitochondrial calcium
1392 uniporter (MCU): molecular identity and physiological roles. The Journal of biological
1393 chemistry 288: 10750-8
1394 Pulli I, Lassila T, Pan G, Yan D, Olkkonen VM, Tornquist K (2018) Oxysterol-binding
1395 protein related-proteins (ORPs) 5 and 8 regulate calcium signaling at specific cell
1396 compartments. Cell calcium 72: 62-69

1397 Rapizzi E, Pinton P, Szabadkai G, Wieckowski MR, Vandecasteele G, Baird G, Tuft RA,
1398 Fogarty KE, Rizzuto R (2002) Recombinant expression of the voltage-dependent anion
1399 channel enhances the transfer of Ca2+ microdomains to mitochondria. The Journal of
1400 cell biology 159: 613-24
1401 Reinisch KM, De Camilli P (2016) SMP-domain proteins at membrane contact sites:
1402 Structure and function. Biochimica et biophysica acta 1861: 924-927
1403 Rizzuto R, Marchi S, Bonora M, Aguiari P, Bononi A, De Stefani D, Giorgi C, Leo S, Rimessi
1404 A, Siviero R, Zecchini E, Pinton P (2009) Ca(2+) transfer from the ER to mitochondria:
1405 when, how and why. Biochimica et biophysica acta 1787: 1342-51
1406 Schikorski T, Young SM, Jr., Hu Y (2007) Horseradish peroxidase cDNA as a marker for
1407 electron microscopy in neurons. Journal of neuroscience methods 165: 210-5
1408 Scorrano L, De Matteis MA, Emr S, Giordano F, Hajnoczky G, Kornmann B, Lackner LL,
1409 Levine TP, Pellegrini L, Reinisch K, Rizzuto R, Simmen T, Stenmark H, Ungermann C,
1410 Schuldiner M (2019) Coming together to define membrane contact sites. Nature
1411 communications 10: 1287
1412 Shiao YJ, Lupo G, Vance JE (1995) Evidence that phosphatidylserine is imported into
1413 mitochondria via a mitochondria-associated membrane and that the majority of
1414 mitochondrial phosphatidylethanolamine is derived from decarboxylation of
1415 phosphatidylserine. The Journal of biological chemistry 270: 11190-8
1416 Shibata Y, Voss C, Rist JM, Hu J, Rapoport TA, Prinz WA, Voeltz GK (2008) The reticulon
1417 and DP1/Yop1p proteins form immobile oligomers in the tubular endoplasmic
1418 reticulum. The Journal of biological chemistry 283: 18892-904
1419 Slot JW, Geuze HJ (2007) Cryosectioning and immunolabeling. Nature protocols 2: 2480-
1420 91
1421 Steenbergen R, Nanowski TS, Beigneux A, Kulinski A, Young SG, Vance JE (2005)
1422 Disruption of the phosphatidylserine decarboxylase gene in mice causes embryonic
1423 lethality and mitochondrial defects. The Journal of biological chemistry 280: 40032-40
1424 Tamura Y, Endo T (2017) Role of Intra- and Inter-mitochondrial Membrane Contact
1425 Sites in Yeast Phospholipid Biogenesis. Advances in experimental medicine and biology
1426 997: 121-133
1427 Tan W, Colombini M (2007) VDAC closure increases calcium ion flux. Biochimica et
1428 biophysica acta 1768: 2510-5
1429 Tasseva G, Bai HD, Davidescu M, Haromy A, Michelakis E, Vance JE (2013)
1430 Phosphatidylethanolamine deficiency in Mammalian mitochondria impairs oxidative
1431 phosphorylation and alters mitochondrial morphology. The Journal of biological
1432 chemistry 288: 4158-73
1433 Tatsuta T, Scharwey M, Langer T (2014) Mitochondrial lipid trafficking. Trends in cell
1434 biology 24: 44-52
1435 Vance JE (1990) Phospholipid synthesis in a membrane fraction associated with
1436 mitochondria. The Journal of biological chemistry 265: 7248-56
1437 Vance JE (2014) MAM (mitochondria-associated membranes) in mammalian cells: lipids
1438 and beyond. Biochimica et biophysica acta 1841: 595-609
1439 Vance JE, Tasseva G (2013) Formation and function of phosphatidylserine and
1440 phosphatidylethanolamine in mammalian cells. Biochimica et biophysica acta 1831:
1441 543-54
1442 Wang H, Ma Q, Qi Y, Dong J, Du X, Rae J, Wang J, Wu WF, Brown AJ, Parton RG, Wu JW,
1443 Yang H (2019) ORP2 Delivers Cholesterol to the Plasma Membrane in Exchange for
1444 Phosphatidylinositol 4, 5-Bisphosphate (PI(4,5)P2). Mol Cell 73: 458-473 e7

Wideman JG (2015) The ubiquitous and ancient ER membrane protein complex (EMC): tether or not? F1000Res 4: 624

Wideman JG, Balacco DL, Fieblinger T, Richards TA (2018) PDZD8 is not the 'functional ortholog' of Mmm1, it is a paralog. F1000Res 7: 1088

Wiel C, Lallet-Daher H, Gitenay D, Gras B, Le Calve B, Augert A, Ferrand M, Prevarskaya N, Simonnet H, Vindrieux D, Bernard D (2014) Endoplasmic reticulum calcium release through ITPR2 channels leads to mitochondrial calcium accumulation and senescence. Nature communications 5: 3792

Wollweber F, von der Malsburg K, van der Laan M (2017) Mitochondrial contact site and cristae organizing system: A central player in membrane shaping and crosstalk. Biochimica et biophysica acta 1864: 1481-1489

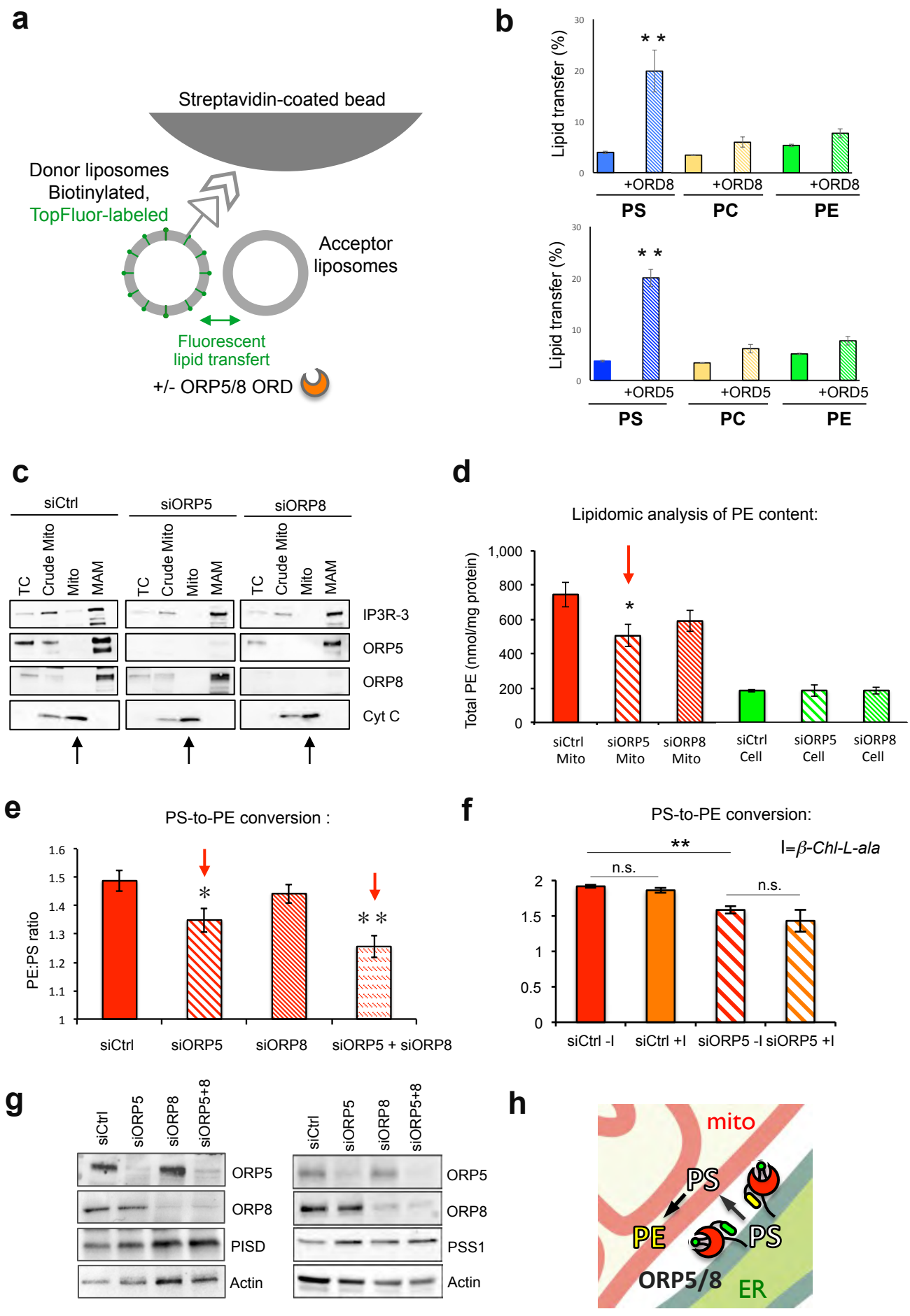
a
Streptavidin-coated bead
Donor liposomes
Biotinylated,
TopFluor-labeled
Acceptor
liposomes
Fluorescent
lipid transfert
+/- ORP5/8 ORD
b
Lipid transfer (%)
+ORD8
+ORD8
+ORD8
PS
PC
PE
Lipid transfer (%)
+ORD5
+ORD5
+ORD5
PS
PC
PE
c
siCtrl
siORP5
siORP8
TC
Crude Mito
Mito
MAM
IP3R-3
ORP5
ORP8
Cyt C
d
Lipidomic analysis of PE content:
Total PE (nmol/mg protein)
siCtrl Mito
siORP5 Mito
siORP8 Mito
siCtrl Cell
siORP5 Cell
siORP8 Cell
e
PS-to-PE conversion :
PE:PS ratio
siCtrl
siORP5
siORP8
siORP5 + siORP8
f
PS-to-PE conversion:
I=β-Chl-L-ala
n.s.
n.s.
siCtrl -I
siCtrl +I
siORP5 -I
siORP5 +I
g
siCtrl
siORP5
siORP8
siORP5+8
ORP5
ORP8
PISD
Actin
PSS1
h
mito
PS
PE
PS
ORP5/8
ER

Figure 1

Figure 1. ORP5 and ORP8 mediate PS transfer *in vitro* and at ER-mitochondria contact sites

(a) Schematic cartoon showing the *in vitro* assay used to study ORP5/8 ORD-mediated lipid transport between liposomes. (b) Donor liposomes containing fluorescent lipids (97 mol% POPC, 1 mol% TopFluor-PS, -PC or -PE and 2 mol% of biotinylated-PE) and pre-bound to streptavidin beads were mixed at a 1:1 molar ratio with acceptor liposomes (100 mol% POPC) in the presence or absence of ORP5 or ORP8 ORD domains (250 μM of donor and acceptor liposomes and 0,3 μM of proteins in the reaction solution). The increase in fluorescence in the acceptor liposomes, which remain unbound in the solution, was measured after 1 hour of incubation at 37°C. Data are presented as % of transferred lipid ±SEM and are the mean of six independent experiments. **P<0,001 (c) Crude mitochondria, mitochondria, and MAM fractions were purified from Ctrl, ORP5 and ORP8 siRNA-treated HeLa cells. Equal amounts of protein from each fraction were loaded on a 4–20% gradient SDS–PAGE gel and immunoblotted using anti-ORP5, anti-ORP8, anti-IP3R-3 (MAM protein), and anti-cytochrome c (mitochondrial protein). Mito, mitochondria; MAM, mitochondria-associated ER membrane. (d) Mass spectrometry (MS)-based quantification of the PE content (nmol/mg protein) of mitochondria isolated from Ctrl, ORP5 or ORP8 knockdown cells and of Ctrl, ORP5 or ORP8 knockdown intact cells. Data are shown as mean of three independent replicates ±SEM. *P<0,05. (e-f) HeLa cells transfected with siCtrl, siORP5, siORP8 or siORP5+ORP8 RNAi oligos were incubated with L-[^{3}H(G)]serine (30.9 Ci/mmol) for 18 hours (e). After extraction and separation of lipids by TLC, PS and PE spots were scraped and analyzed for [^{3}H] radioactivity, as described under “Methods”. Each condition was analyzed in triplicate in each of three independent biological replicates. Data are presented as mean of PE:PS ratio ±SEM. *P<0,05, **P<0,01 compared to Ctrl. (f) Cells transfected with siCtrl and siORP5 oligos were treated with b-Chloro-L-alanine (b-Chl-L-ala, inhibitor of Ser-palmitoyltransferase) or untreated, then pulsed with 15 μCi/ml of [^{3}H(G)]serine for 1 hour and chased for 12 hours in serum-free DMEM, before analysis. n.s. not significant, **P<0,01 compared to Ctrl. (g) WB analysis showing ORP5, ORP8, PSD1, PSS1 and Actin levels in protein lysates from HeLa cells treated with either Ctrl siRNAs or with siRNAs against ORP5 or/and ORP8. (h) Schematic representation of non-vesicular PS transfer mediated by ORP5/8 at ER-mitochondria contact sites. PS is transported to mitochondrial membranes where it is rapidly converted into mitochondrial PE.

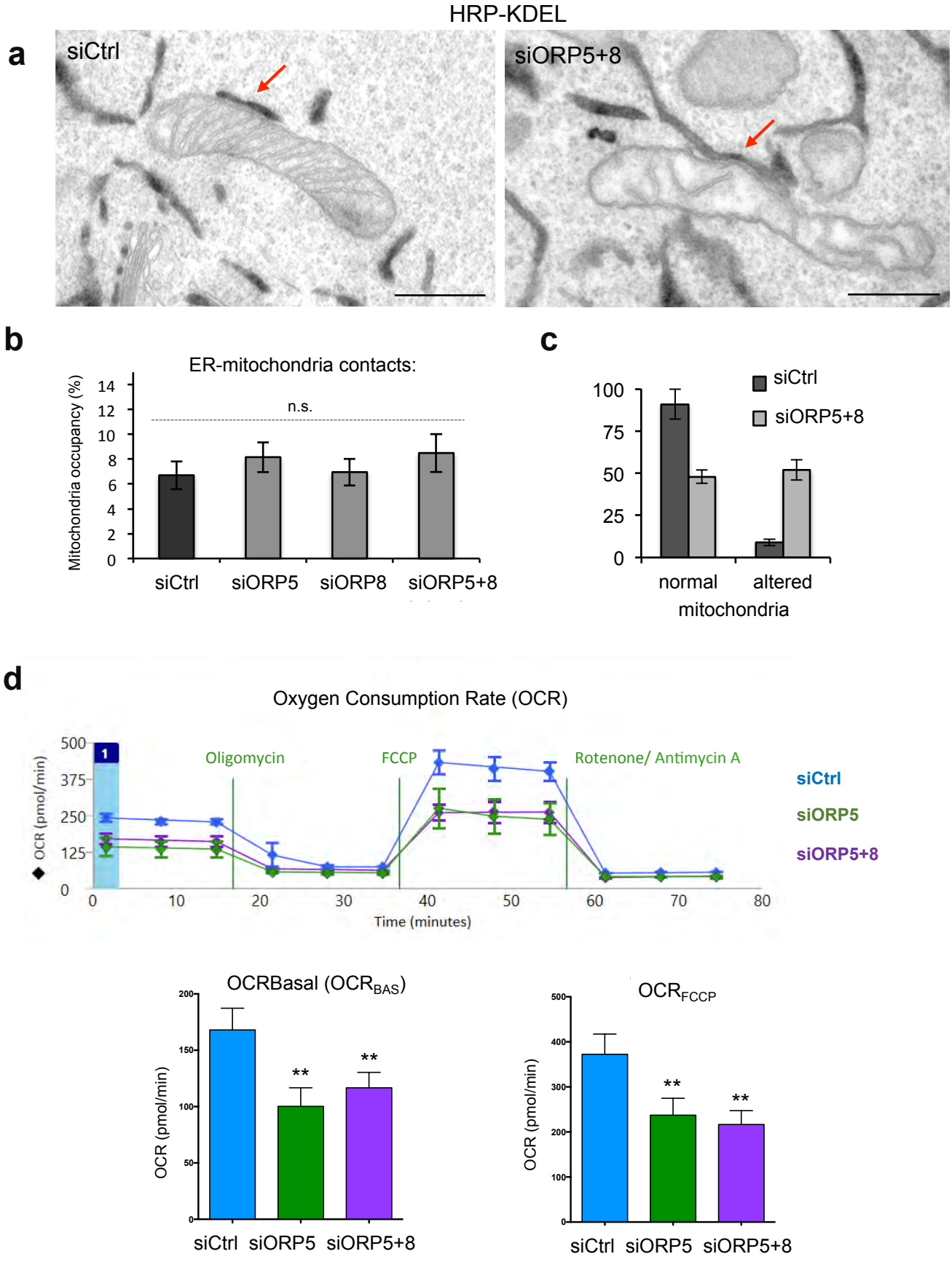
HRP-KDEL
a
siCtrl
siORP5+8
b
ER-mitochondria contacts:
Mitochondria occupancy (%)
n.s.
siCtrl
siORP5
siORP8
siORP5+8
c
siCtrl
siORP5+8
normal
altered
mitochondria
d
Oxygen Consumption Rate (OCR)
OCR (pmol/min)
Oligomycin
FCCP
Rotenone/ Antimycin A
Time (minutes)
siCtrl
siORP5
siORP5+8
OCRBasal (OCR$_{BAS}$)
OCR$_{FCCP}$
**

Figure 2

Figure 2. ORP5 and ORP8 knockdown affect mitochondria morphology and respiratory function but not the aboundance of ER-mitochondria contact sites

(a) Electron micrographs of HRP-KDEL-expressing HeLa cells treated with Ctrl siRNAs (siCtrl) or siRNAs against ORP5 and ORP8 (siORP5+siORP8). Red arrows indicate ER-mitochondria contact sites. Scale bar, 500 nm. (b) Quantifications of the extent of ER-mitochondria contact sites in siCtrl, siORP5, siORP8 and siORP5+8 cells expressing HRP-KDEL. Data are shown as % of the ER in contact with mitochondria (mitochondria occupancy) ±SEM, n = 20 cell profiles and ±900 mitochondria; n.s; not significant. (c) Quantifications of the number of mitochondria with aberrant cristae morphology in the indicated siRNA conditions. Data are shown as % of mitochondria ±SEM, n = 20 cell profiles and ±700 mitochondria. **P<0,01 compared to siCtrl. (d) Mitochondrial oxygen consumption rate (OCR) measured in Ctrl, ORP5 or ORP8, and ORP5+8 siRNA-treated HeLa cells. OCR trace was obtained by sequential measurement of basal OCR (OCR_{BAS}), OCR after the addition of Oligomycin, OCR after the addition of FCCP (OCR_{FCCP}) and OCR after the addition of Rotenone/Antimycin A. Note the reduced OCR in siORP5 and siORP5+8 cells compared to Ctrl siRNA cells. Error bars denote ±SEM. Data shown in the bar charts are the mean of 4 independent repeats (n=4). **P<0,01 compared to Ctrl.

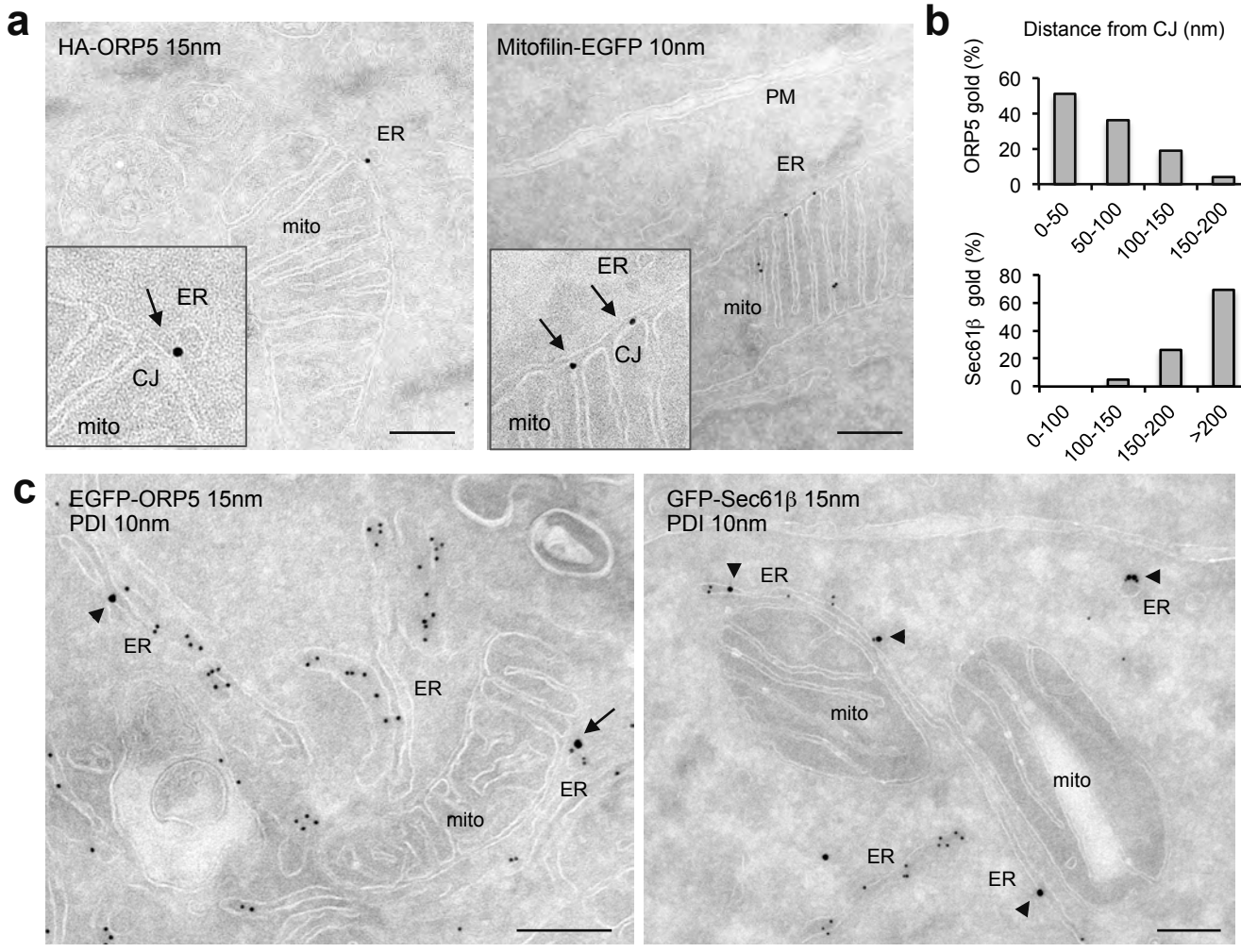

Figure 3. ORP5 localize at ER-mitochondria contact sites near cristae junctions (CJ)

(a) Electron micrographs of ultrathin cryosections of HeLa cells transfected with HA-ORP5 or Mitofilin-EGFP and immunogold stained with anti-HA or anti-GFP (10 or 15 nm gold), showing ORP5 localization at ER-mitochondria contacts in close proximity to CJ (arrow) and the localization of the MICOS complex (Mitofilin) at CJ (arrows). Scale bar 250 nm. (b) Quantification of the proximity of HA-ORP5 and EGFP-Sec61β gold particles to the CJ. Results are presented as the percentage of ORP5 or Sec61β gold particles (n = 23 cell profiles) at specific ranges of distance (in nm) from CJ. (c) Electron micrographs of ultrathin cryosections of HeLa cells transfected with EGFP-ORP5 or GFP-Sec61β and immunogold labeled with anti-GFP (15 nm gold) and anti-PDI (10nm gold). Note ORP5 localization at ER-mitochondria contacts near CJ (arrow) and Sec61β localization to ER membranes not in contact with the mitochondria membranes (arrowheads). Scale bar 250 nm.

Figure 3

a

Mass-Spectrometry Analysis

		IP EGFP	IP EGFP-ORP5	IP EGFP-ORP5ΔPH
Protein	**Localization**	**Mascot Score**		
ORP5	MAMs	0	9689	12192
ORP8	MAMs	31	930	690
Mitofilin	IMM	43	579	1150
SAM50	OMM	0	237	516
Metaxin2	OMM	0	32	175
RHOT2	OMM	0	131	119
TOM22	OMM	0	77	95
PTPIP51	OMM	0	76	73

b

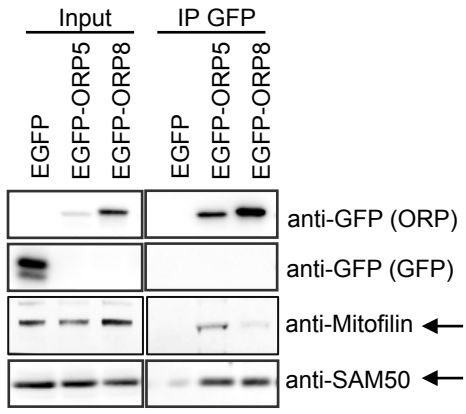

c

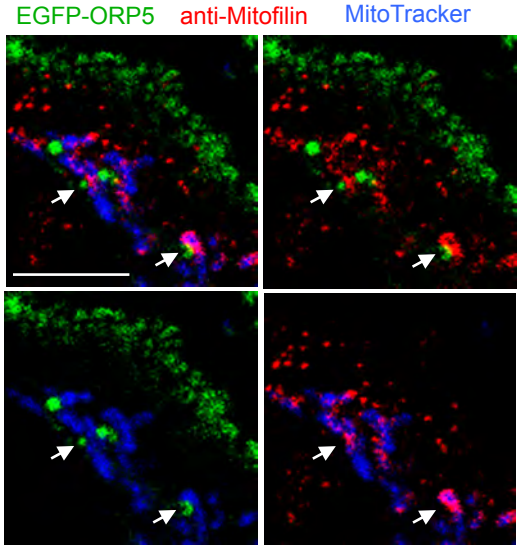

d

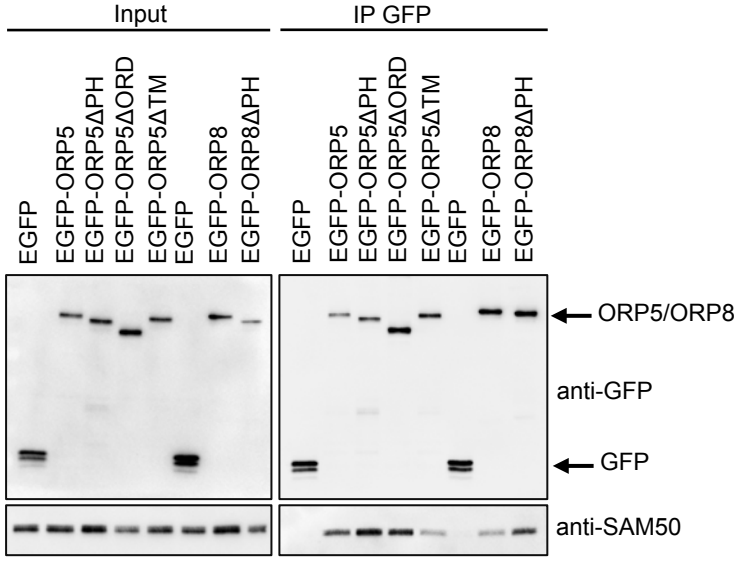

e

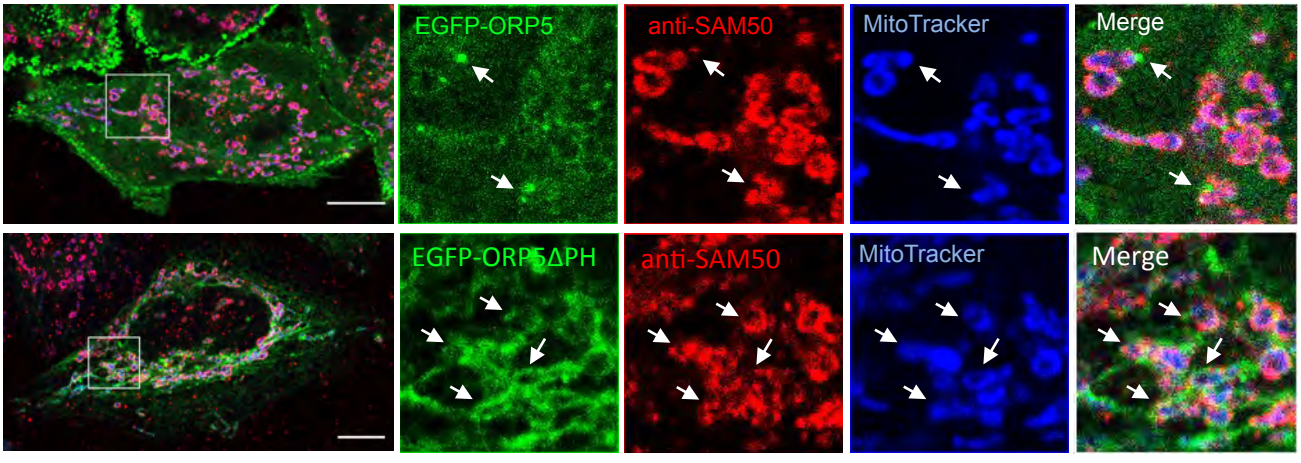

Figure 4

Figure 4. ORP5 and ORP8 interact with the MIB/MICOS complex at ER-mitochondria contacts near CJ

(a) Identification of mitochondrial proteins associated to mitochondrial outer or inner membranes (OMM, IMM) that interact with EGFP-tagged ORP5 constructs by mass spectrometry. Note the presence of some proteins of the MIB complex: Mitofilin, SAM50 and Metaxin2. Interaction scores (Mascot scores) of Mitofilin, SAM50 and Metaxin2 with the EGFP-ORP5ΔPH construct are stronger than with EGFP-ORP5. (b) EGFP-ORP5, EGFP-ORP8 or EGFP alone were transfected in HeLa cells then immuno-precipitated from lysates and analyzed by western blot using antibodies against GFP (for ORP5 or ORP8), Mitofilin or SAM50. (c) Confocal images of a region of HeLa cells transfected with EGFP-ORP5 (green) and stained with MitoTracker (blue) and anti-Mitofilin (red) antibody. Arrows point to ORP5-positive ER elements in proximity to mitofilin-enriched microdomains on mitochondria. Scale bar, 5 μm. (d) EGFP-ORP5, EGFP-ORP5ΔPH, EGFP-ORP5ΔORD, EGFP-ORP5ΔTM, EGFP-ORP8, EGFP-ORP8ΔPH or EGFP alone were transfected in HeLa cells then immuno-precipitated from lysates and analyzed by western blot using antibodies against GFP (for ORP5 or ORP8) or against SAM50. (e) Confocal images of HeLa cells transfected with either EGFP-ORP5 or EGFP-ORP5ΔPH (green) and stained with MitoTracker (Blue) and anti-SAM50 (red) antibody. Arrows point to ORP5-positive ER elements in proximity to SAM50-positive mitochondria. Insets show magnifications of the boxed regions. Scale bar, 10 μm.

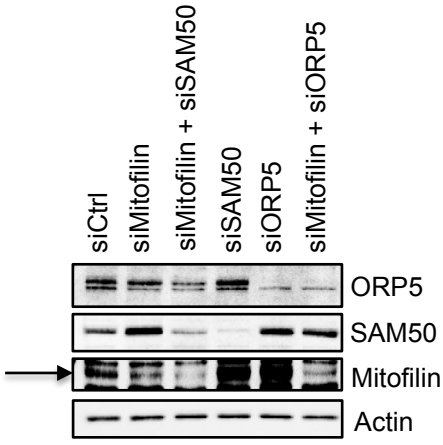
a
siCtrl
siMitofilin
siMitofilin + siSAM50
siSAM50
siORP5
siMitofilin + siORP5
ORP5
SAM50
Mitofilin
Actin

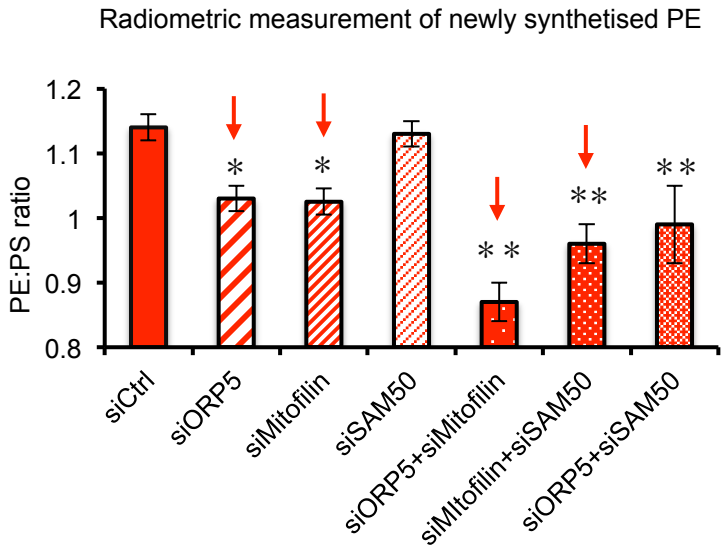
b
Radiometric measurement of newly synthetised PE
PE:PS ratio
1.2
1.1
1
0.9
0.8
siCtrl
siORP5
siMitofilin
siSAM50
siORP5+siMitofilin
siMltofilin+siSAM50
siORP5+siSAM50

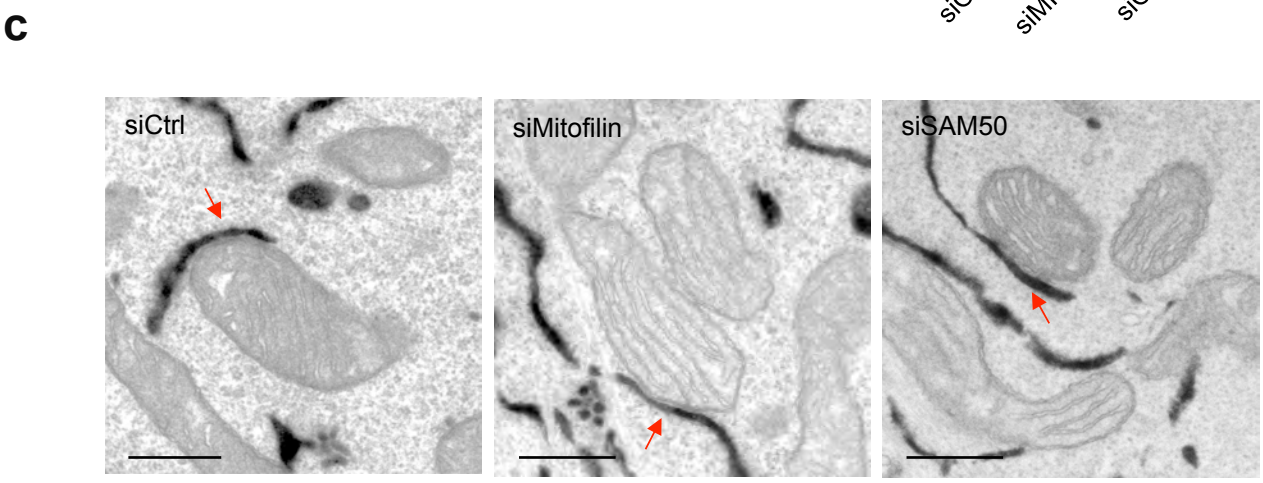
c
siCtrl
siMitofilin
siSAM50

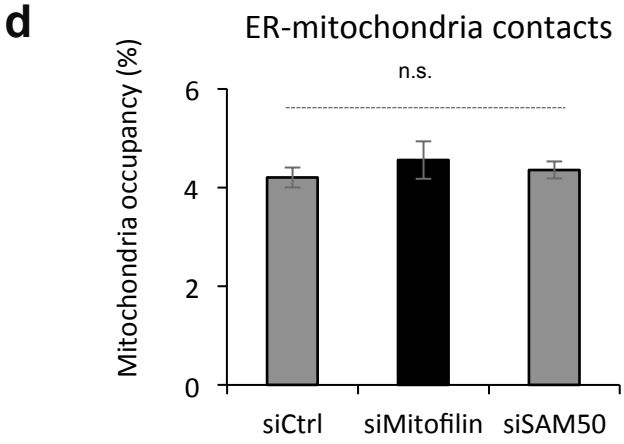
d
ER-mitochondria contacts
n.s.
Mitochondria occupancy (%)
6
4
2
0
siCtrl
siMitofilin
siSAM50

Figure 5

Figure 5. ORP5 and the MIB/MICOS complex cooperate to mediate non-vesicular transport of PS from the ER to mitochondrial membranes

(a) Western analysis showing ORP5, SAM50, Mitofilin and Actin levels in protein lysates from HeLa cells treated with siRNA against Ctrl, ORP5, Mitofilin or SAM50. Arrow indicates the specific band for Mitofilin. (b) Radiometric measurement of PS-to-PE conversion in the indicated siRNAs. Data are presented as mean of PE:PS ratio ±SEM. Each condition was performed in triplicate in each of the independent biological replicates (n = 5 for siCtrl and siORP5; n = 4 for siSAM50; n = 3 for the other siRNAs conditions). *P<0,05, **P<0,01 compared to Ctrl. (c) Representative electron micrographs of HeLa cells treated with Ctrl siRNAs or siRNAs against Mitofilin or SAM50 and transfected with HRP-KDEL. Red arrows indicate ER-mitochondria contact sites. Scale bar, 500 nm. (d) Quantifications of the extent of ER-mitochondria contact sites in Ctrl, Mitofilin and SAM50 knockdown cells expressing HRP-KDEL. Data are shown as % of the ER in contact with mitochondria (mitochondria occupancy) ±SEM, n = 30 for siCtrl, n = 20 cell profiles for siMitofilin and siSAM50 and 1 000 mitochondria; n.s; not significant.

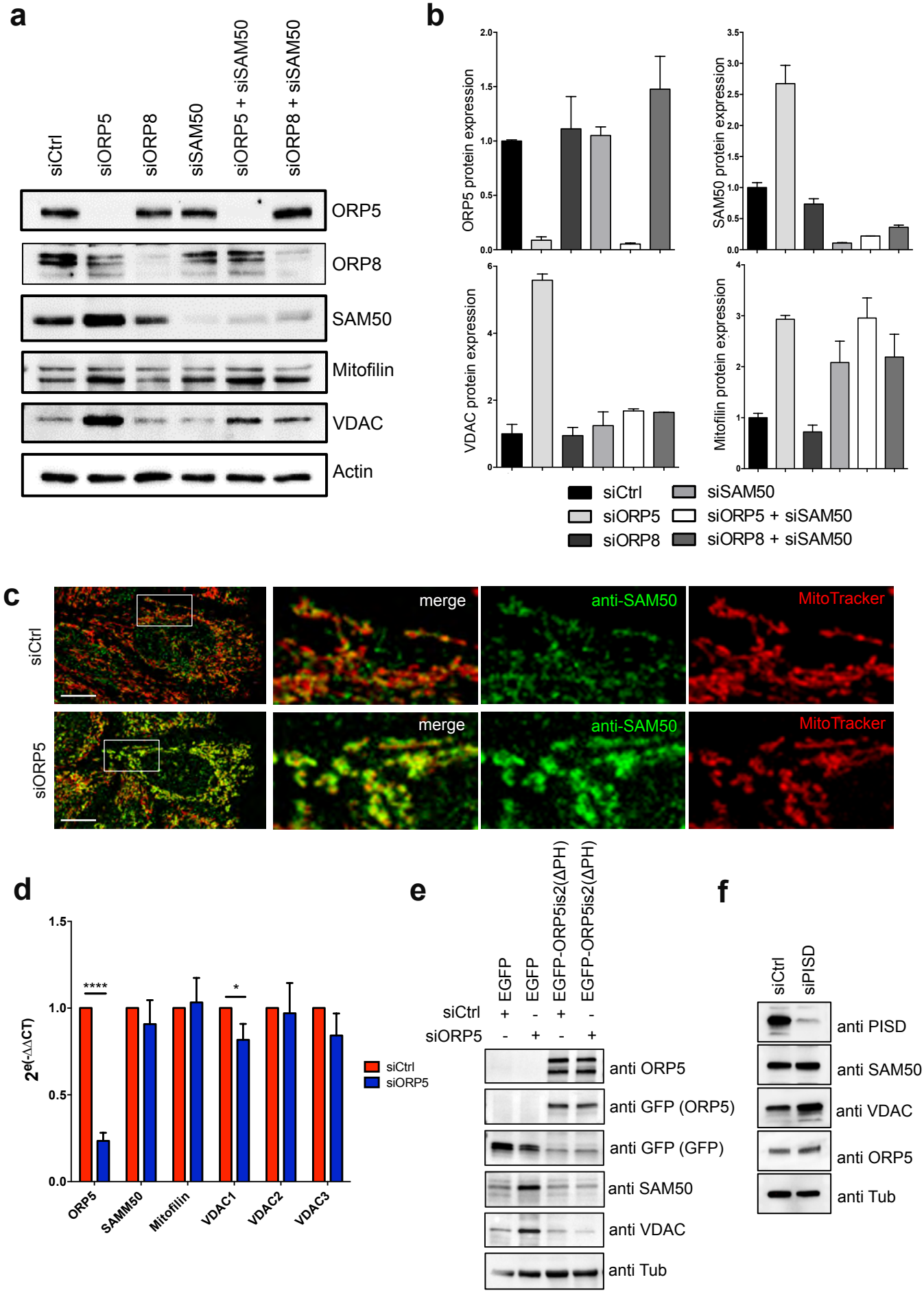
a
siCtrl
siORP5
siORP8
siSAM50
siORP5 + siSAM50
siORP8 + siSAM50
ORP5
ORP8
SAM50
Mitofilin
VDAC
Actin
b
ORP5 protein expression
SAM50 protein expression
VDAC protein expression
Mitofilin protein expression
siCtrl
siORP5
siORP8
siSAM50
siORP5 + siSAM50
siORP8 + siSAM50
c
siCtrl
siORP5
merge
anti-SAM50
MitoTracker
d
2^(-ΔΔCT)
****
*
ORP5
SAMM50
Mitofilin
VDAC1
VDAC2
VDAC3
siCtrl
siORP5
e
EGFP
EGFP
EGFP-ORP5is2(ΔPH)
EGFP-ORP5is2(ΔPH)
siCtrl
siORP5
anti ORP5
anti GFP (ORP5)
anti GFP (GFP)
anti SAM50
anti VDAC
anti Tub
f
siCtrl
siPISD
anti PISD
anti SAM50
anti VDAC
anti ORP5
anti Tub

Figure 6

Figure 6. Silencing of ORP5 but not ORP8 specifically increases VDAC protein level in a SAM50-dependent manner

(a) Western analysis showing ORP5, ORP8, SAM50, Mitofilin, VDAC and Actin levels in protein lysates from HeLa cells treated with either Ctrl siRNAs, or with siRNAs against ORP5, ORP8, or SAM50. (b) Quantification of ORP5, SAM50, VDAC and Mitofilin protein expression in the indicated knockdown conditions. Normalized data are shown as mean ±SEM (n = 3). (c) Confocal images of Ctrl and ORP5 knockdown HeLa cells labeled with MitoTracker (red) and immunostained using anti-SAM50 antibody (green). Scale bar, 10 µm. (d) Quantitative RT-PCR analysis of ORP5, SAM50, Mitofilin, VDAC1, VDAC2 and VDAC3 in ORP5 knockdown cells versus control HeLa cells. y axis: $2^{(-\Delta\Delta Ct)}$ value represents differences between the mean Ct (Cycle threshold) values of tested genes and those of reference gene (SDHA). (e) HeLa cells treated with siRNA against Ctrl and ORP5, were transfected with EGFP alone or with EGFP-ORP5is2 (ORP5 isoform 2) and cell lysates following SDS-PAGE were immunoblotted with antibodies against GFP (to detect EGFP and EGFP-ORP5), ORP5, SAM50, VDAC and Tubulin. Note the rescue of SAM50 and VDAC levels in siORP5 cells transfected with EGFP-ORP5is2 as compared to cells expressing EGFP alone. (f) Western analysis showing PISD, SAM50, VDAC, ORP5 and Tubulin levels in protein lysates from HeLa cells treated with either Ctrl siRNAs, or with siRNAs against PISD.

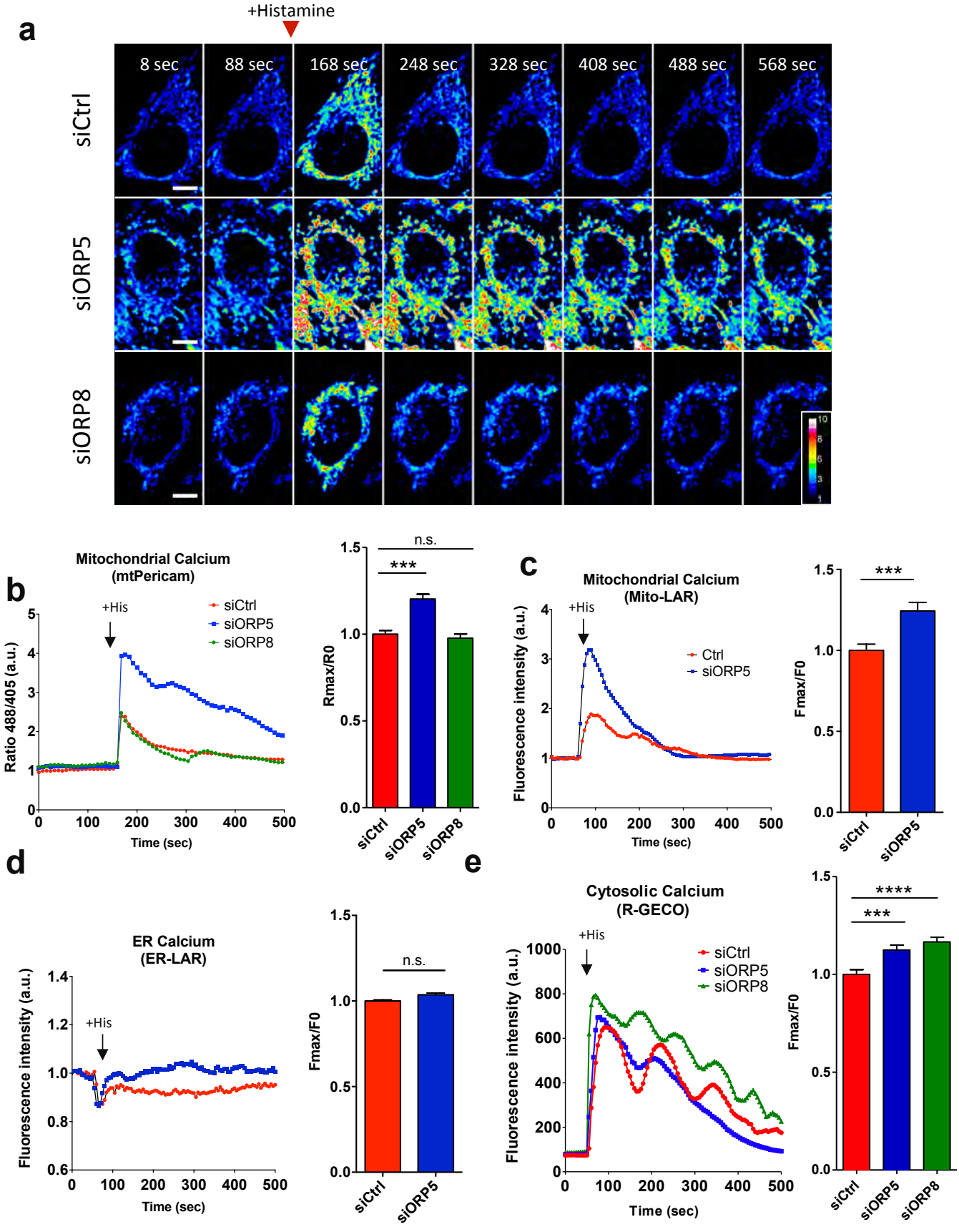
a
+Histamine
8 sec
88 sec
168 sec
248 sec
328 sec
408 sec
488 sec
568 sec
siCtrl
siORP5
siORP8
b
Mitochondrial Calcium
(mtPericam)
+His
siCtrl
siORP5
siORP8
Ratio 488/405 (a.u.)
Time (sec)
Rmax/R0
n.s.
***
c
Mitochondrial Calcium
(Mito-LAR)
Ctrl
siORP5
Fluorescence intensity (a.u.)
Fmax/F0
d
ER Calcium
(ER-LAR)
e
Cytosolic Calcium
(R-GECO)
****

Figure 7

Figure 7. Silencing of ORP5 but not ORP8 increases mitochondrial calcium

(a) Pseudocolor 488/405 ratio time-lapse images of a representative Ctrl, ORP5 or ORP8 knockdown HeLa cell expressing mt-Pericam before and after histamine treatment. Scale bar 10 μm. (b) Representative curves of Ctrl, ORP5 and ORP8 knockdown HeLa cells expressing mt-Pericam showing the ratio of Pericam fluorescence before and after histamine treatment (+His). The change in the ratio of Pericam fluorescence after histamine treatment under each condition was compared (Rmax/R0). Data are presented as normalized mean ±SEM, n = 3 per condition, ***, $p < 0.001$; n.s; not significant. (c) Representative curves of Ctrl and ORP5 knockdown HeLa cells expressing the GECO construct Mito-LAR showing the fluorescence before and after histamine treatment. The change in fluorescence after histamine treatment under each condition was compared (Fmax/F0). Data are presented as normalized mean ±SEM, n = 3 per condition, ***, $p < 0.001$; n.s; not significant. (d) Representative curves of Ctrl and ORP5 knockdown HeLa cells expressing the GECO construct ER-LAR showing the fluorescence before and after histamine treatment. The change in fluorescence after histamine treatment under each condition was compared (Fmax/F0). Data are presented as normalized mean ±SEM, n = 3 per condition, n.s; not significant. (e) Representative curves of Ctrl, ORP5 and ORP8 knockdown HeLa cells expressing the GECO construct R-GECO showing the fluorescence before and after histamine treatment. The change in fluorescence after histamine treatment under each condition was compared (Fmax/F0). Data are presented as normalized mean ±SEM, n = 3 per condition, ***, $p < 0.001$ and ****, $p < 0.0001$; n.s; not significant.

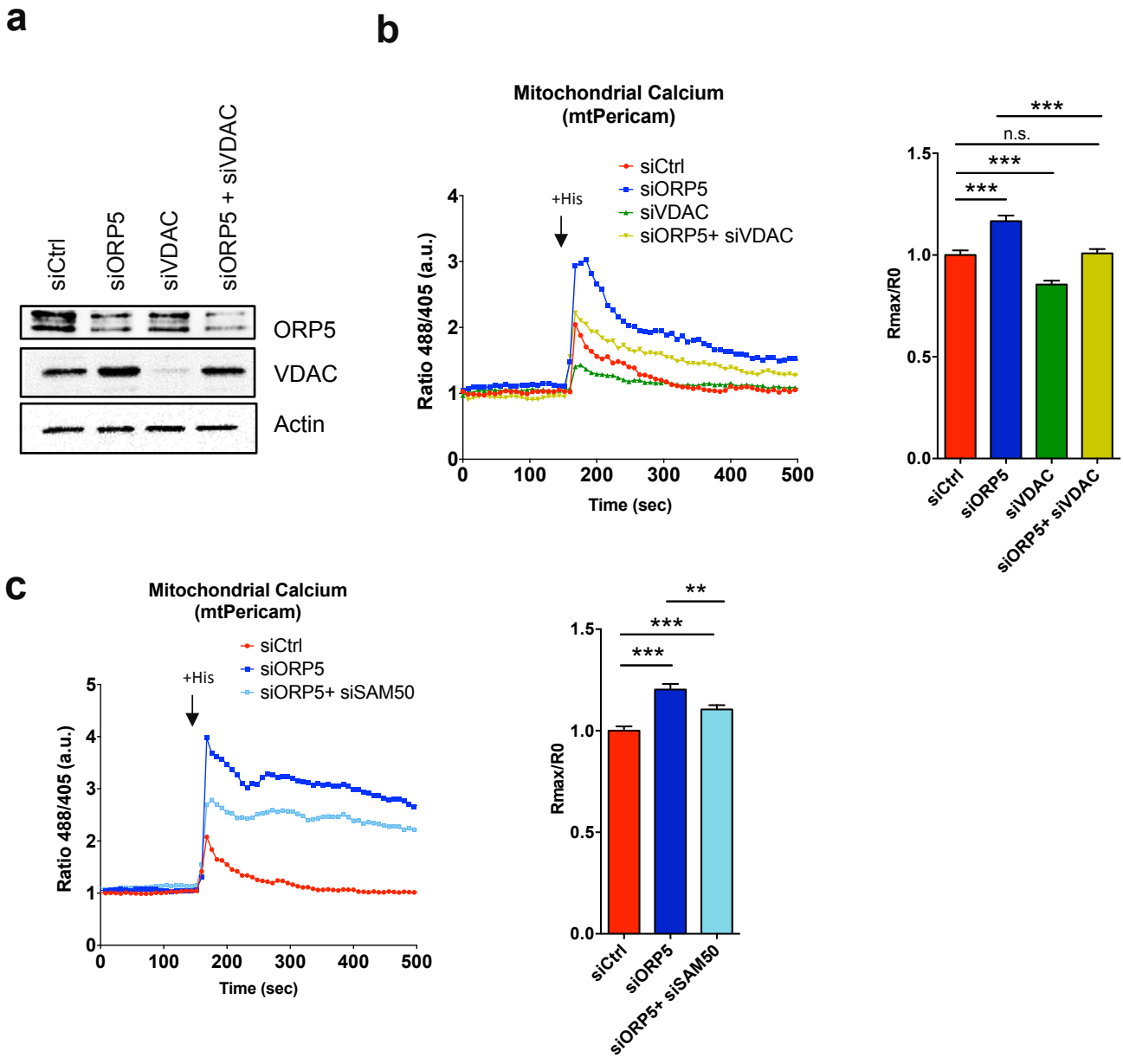
a
siCtrl
siORP5
siVDAC
siORP5 + siVDAC
ORP5
VDAC
Actin
b
Mitochondrial Calcium
(mtPericam)
+His
siCtrl
siORP5
siVDAC
siORP5+ siVDAC
Ratio 488/405 (a.u.)
Time (sec)
0
100
200
300
400
500
0
1
2
3
4
***
n.s.
***
***
1.5
1.0
0.5
0.0
Rmax/R0
siCtrl
siORP5
siVDAC
siORP5+ siVDAC
c
Mitochondrial Calcium
(mtPericam)
+His
siCtrl
siORP5
siORP5+ siSAM50
Ratio 488/405 (a.u.)
Time (sec)
0
100
200
300
400
500
0
1
2
3
4
5
**
***
***
1.5
1.0
0.5
0.0
Rmax/R0
siCtrl
siORP5
siORP5+ siSAM50

Figure 8

Figure 8. Calcium increase induced by ORP5 knockdown is dependent on SAM50 and VDAC

(a) Western analysis showing ORP5 and VDAC protein levels in Ctrl, ORP5 and VDAC siRNA-treated HeLa cells. (b). Representative curves of Ctrl, ORP5, VDAC and ORP5+VDAC knockdown HeLa cells expressing mt-Pericam showing the ratio of Pericam fluorescence before and after histamine treatment (+His). The change in the ratio of Pericam fluorescence after histamine treatment under each condition was compared (Rmax/R0). Data are presented as normalized mean ±SEM, n = 3 per condition, ***, $p < 0.001$; n.s; not significant. (c). Representative curves of Ctrl, ORP5 and ORP5+SAM50 knockdown HeLa cells expressing mt-Pericam showing the ratio of Pericam fluorescence before and after histamine treatment (+His). The change in the ratio of Pericam fluorescence after histamine treatment under each condition was compared (Rmax/R0). Data are presented as normalized mean ±SEM, n = 3 per condition, ***, $p < 0.001$; n.s; not significant.

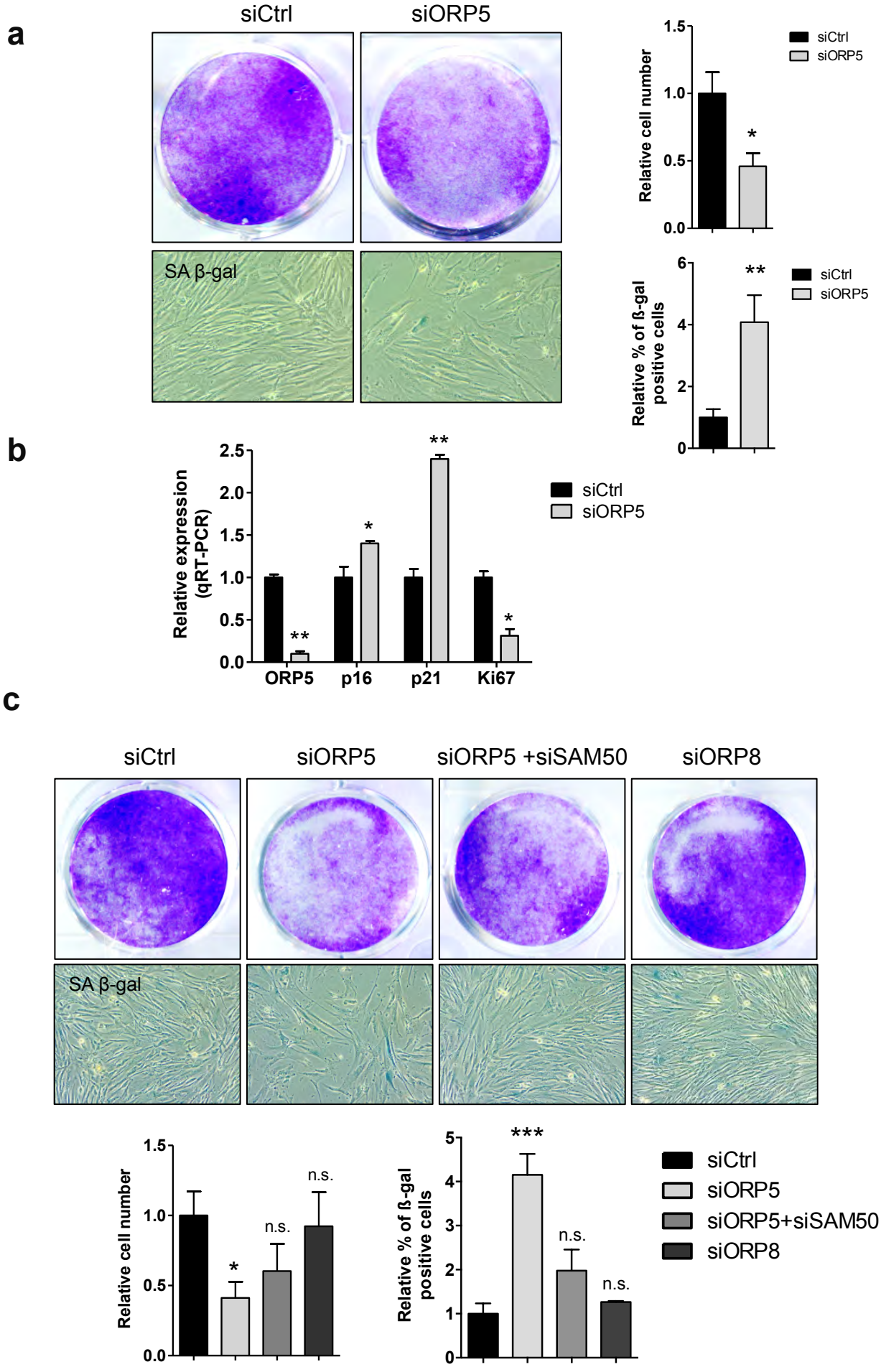
a
siCtrl
siORP5
SA β-gal
Relative cell number
1.5
1.0
0.5
0.0
*
siCtrl
siORP5
Relative % of ß-gal positive cells
6
4
2
0
**
siCtrl
siORP5
b
Relative expression (qRT-PCR)
2.5
2.0
1.5
1.0
0.5
0.0
**
*
**
*
ORP5
p16
p21
Ki67
siCtrl
siORP5
c
siCtrl
siORP5
siORP5 +siSAM50
siORP8
SA β-gal
Relative cell number
1.5
1.0
0.5
0.0
*
n.s.
n.s.
Relative % of ß-gal positive cells
5
4
3
2
1
0
***
n.s.
n.s.
siCtrl
siORP5
siORP5+siSAM50
siORP8

Figure 9

Figure 9. Cell senescence promoted by ORP5 knockdown is dependent on SAM50

(a) MCR5 cells transfected with control siRNA or with siRNA against ORP5 were fixed and then stained with crystal violet solution (CA) or with SA-β-galactosidase (SA-β-Gal) staining solution. The graph on the top right shows the relative cell number determined by crystal violet staining. The graph on the bottom right shows the relative percentage of β-gal positive cells determined by SA-β-galactosidase assay. Data are presented as normalized mean ±SEM, n = 3 per condition, **, $p< 0.01$; *, $p< 0.05$. (b) Quantitative RT-PCR analysis of ORP5, p16, p21 and Ki67 in ORP5 knockdown cells and control HeLa cells. y axis:$2^{(-\Delta\Delta Ct)}$ value represents differences between the mean Ct (Cycle threshold) values of tested genes and those of reference genes (PGK1 and HPRT1). Data are presented as normalized mean ±SEM, n = 3 per condition, **, $p< 0.01$; *, $p< 0.05$. (c) MCR5 cells transfected with control siRNA or with siRNA against ORP5, SAM50 or ORP8 were fixed and then stained with crystal violet solution or with SA-β-Gal staining solution. The graph on the left shows the relative cell number determined by crystal violet staining. The graph on the right shows the relative percentage of β-gal positive cells determined by SA-β-galactosidase assay. Data are presented as normalized mean ±SEM, n = 3 per condition, ***, $p< 0.001$; *, $p< 0.05$; n.s; not significant.

a

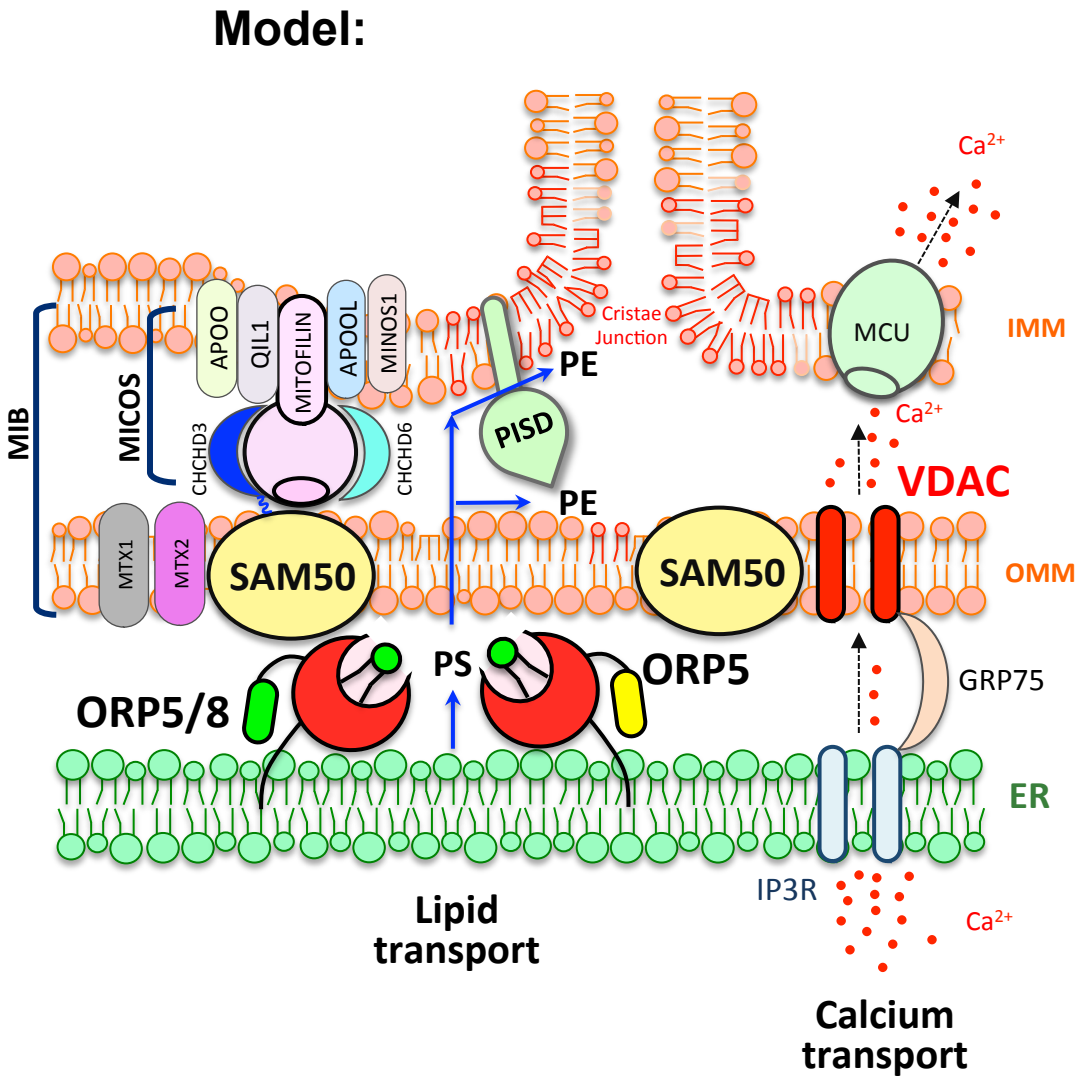

Figure 10. Lipid and calcium transport occur at the same ER-mitochondria contact site microdomains and are regulated by a ORP5-SAM50-VDAC pathway

ORP5/8 are directly involved in the transfer of PS from ER to mitochondria at ER-mitochondria membrane contact sites. This transfer occurs at the level of cristae junctions (CJ) where ORP5/8 localize and interacts with the proteins of the MIB complex SAM50 and Mitofilin. This interaction facilitates the transfer of PS from ER to the mitochondrial membranes at the level of CJ and PS conversion into PE, a phospholipid that plays a critical role in cristae organization and mitochondrial function. ORP5 is also involved in calcium homeostasis by regulating the level of VDAC *via* modulation of SAM50 protein levels.

Figure 10

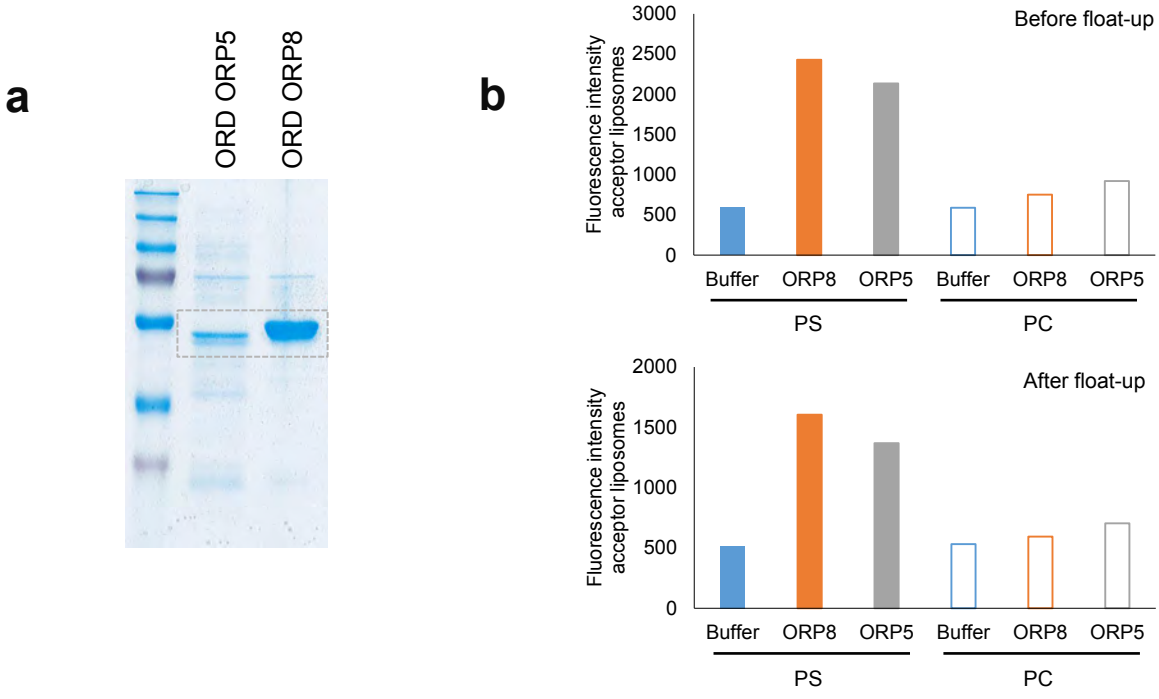

Figure S1. (a) Coomassie stained SDS-PAGE of the recombinant ORD domain of ORP5/8 proteins purified in BL21DE3 RILP cells. (b) Results of a lipid transfer experiment performed as in Fig. 1 a, b and presented as the fluorescence intensity of acceptor liposomes before (top panel) or after (bottom panel) their floatation on a Nycodenz gradient to confirm that fluorescence comes from the liposomes membrane.

Figure S1

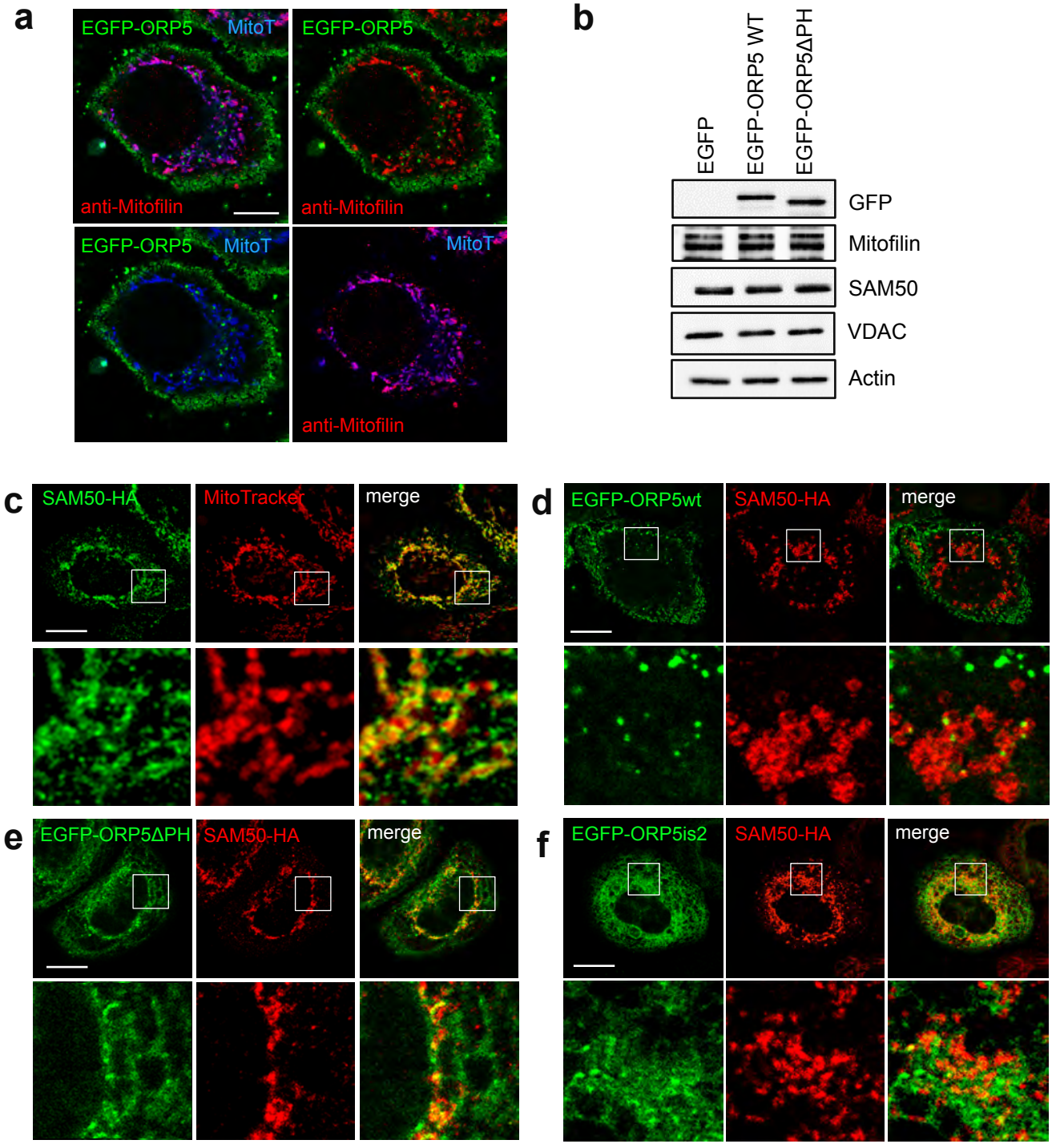
a
EGFP-ORP5
MitoT
anti-Mitofilin
EGFP-ORP5
anti-Mitofilin
EGFP-ORP5
MitoT
MitoT
anti-Mitofilin
b
EGFP
EGFP-ORP5 WT
EGFP-ORP5ΔPH
GFP
Mitofilin
SAM50
VDAC
Actin
c
SAM50-HA
MitoTracker
merge
d
EGFP-ORP5wt
SAM50-HA
merge
e
EGFP-ORP5ΔPH
SAM50-HA
merge
f
EGFP-ORP5is2
SAM50-HA
merge

Figure S2

Figure S2. (a**)** Confocal micrograph of a HeLa cell (corresponding to boxed region in Fig 4c) transfected with EGFP-ORP5 (green) and stained with MitoTracker (blue) and anti-Mitofilin (red) antibody. Scale bar, 10 μm. (b) WB analysis showing GFP (EGFP-tagged constructs), Mitofilin, VDAC and SAM50 and Actin levels in protein lysates from HeLa cells transfected with either EGF construct (Control) or with EGFP-ORP5 or EGFP-ORP5ΔPH constructs. (c) Confocal images of a HeLa cell transfected with SAM50-HA and stained with HA antibody to detect SAM50 (green) and MitoTracker to label mitochondria (red). Insets show magnifications of the boxed regions. Scale bar, 10 μm. (d-f) Confocal images of HeLa cells transfected with EGFP-ORP5, EGFP-ORP5ΔPH or EGFP-ORP5is2 (green) together with SAM50-HA and stained with HA antibody to detect SAM50 (red). Insets show magnifications of the boxed regions. Scale bar, 10 μm.

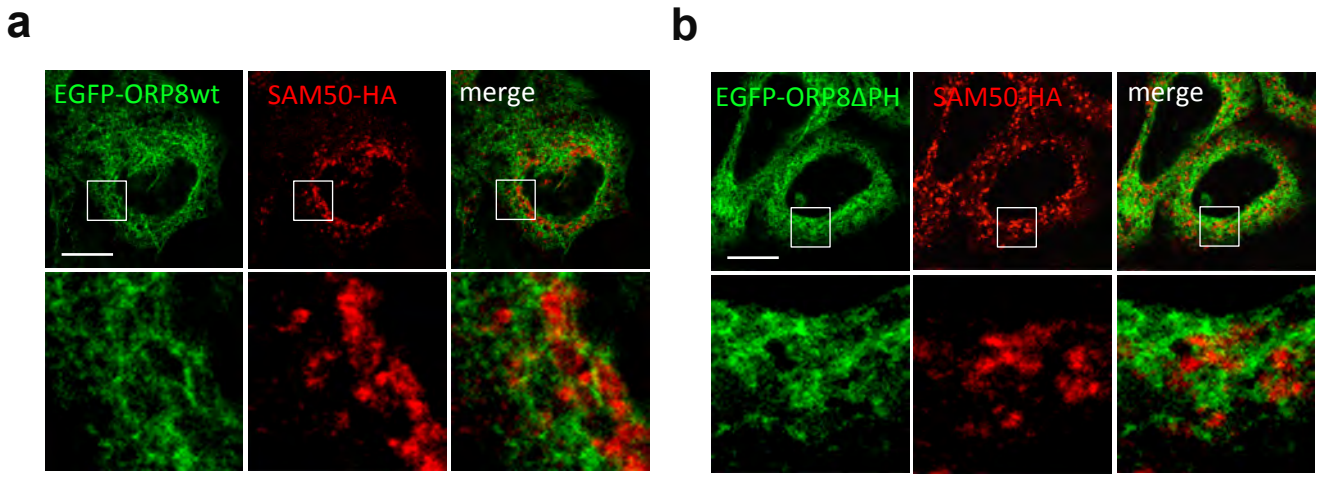

Figure S3. (a-b) Confocal images of HeLa cell co-transfected with EGFP-ORP8 (a) or EGFP-ORP8ΔPH (b) (green) and SAM50-HA, immunostained with anti-HA to detect SAM50 (red). Insets show magnifications of the boxed regions. Scale bar, 10 μm.

Figure S3

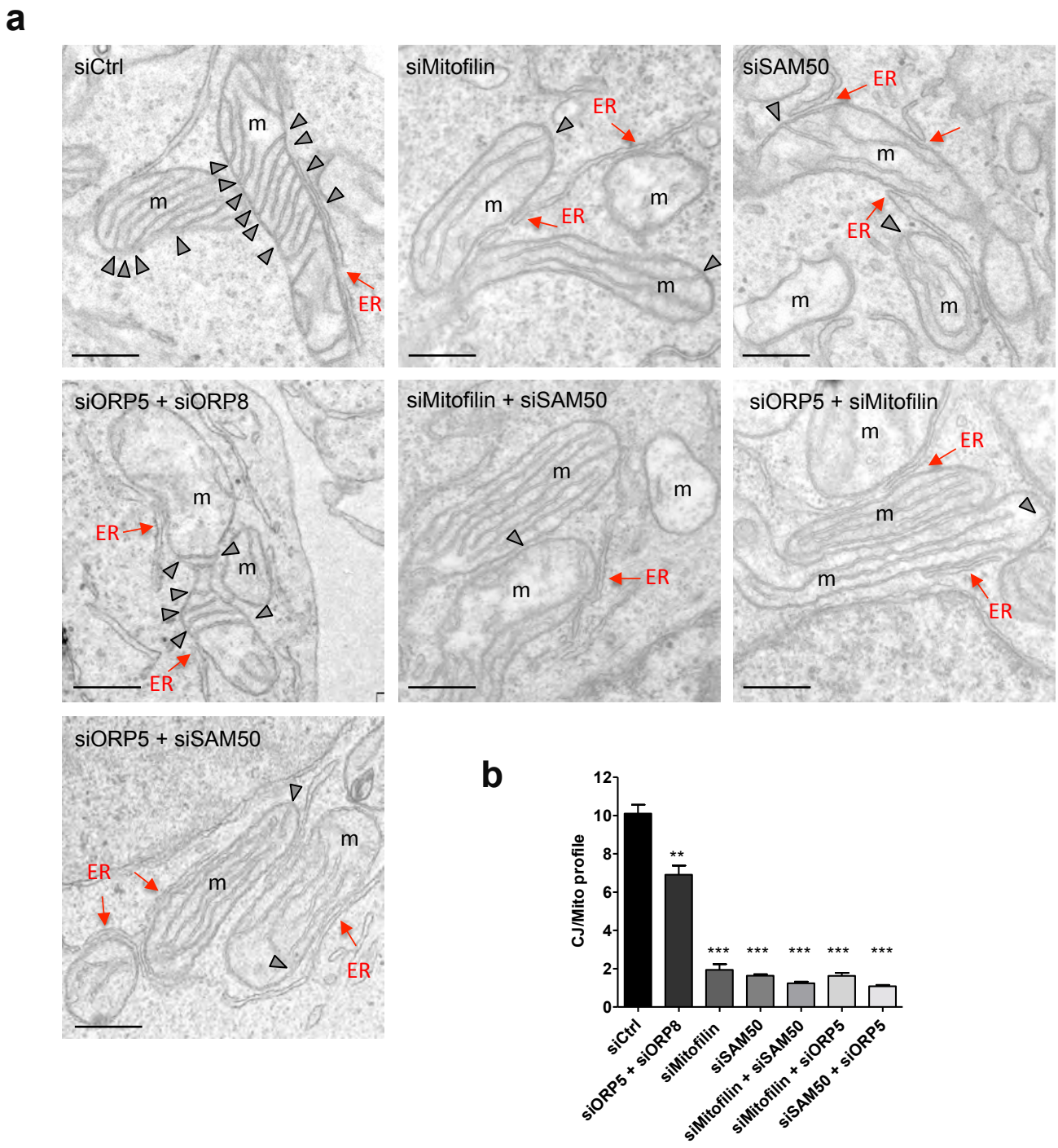

Figure S4. (a) Representative EM micrographs showing the morphology of mitochondria in HeLa cells treated with siRNA against ORP5, ORP8, Mitofilin and SAM50. Scale bar, 200 nm. Red arrows indicate ER elements in contact with mitochondria; arrowheads indicate CJ; m, mitochondria. (b) Quantifications of the number of CJ per mitochondria profile in the indicated siRNA conditions. % of CJ ±SEM, n = 170-260 mitochondria, ***, p< 0.001; **, p< 0.01.

Figure S4

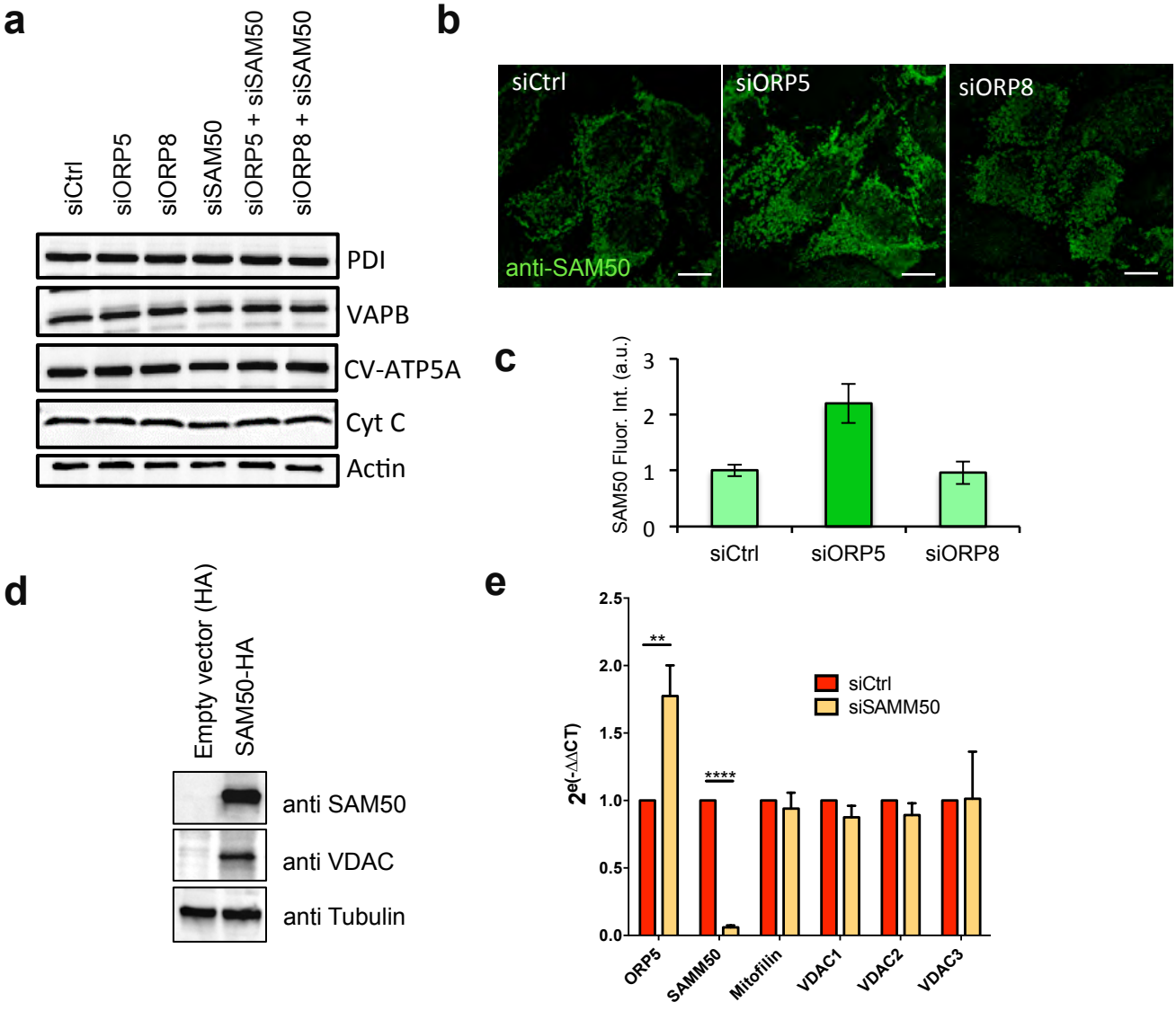

Figure S5. (a) WB analysis showing PDI (ER), VAPB (ER), CV-ATP5A (IMM), Cytochrome C (Cyt C, IMM) and Actin levels in protein lysates from HeLa cells treated with either Ctrl siRNAs or with siRNAs against ORP5, ORP8, or SAM50. (b) Confocal images of Ctrl, ORP5 and ORP8 knockdown HeLa cells immunostained using anti-SAM50 antibody (green). Scale bar, 10 µm. (c) Quantification of fluorescent intensity in SAM50-labelled cells. Normalized data from three independednt replicates are presented. Error bars denote ±SEM (d) WB analysis showing SAM50, VDAC and Tubulin levels in protein lysates from HeLa cells treated with either SAM50-HA or an empty vector. (e) Quantitative RT-PCR analysis of ORP5, SAM50, Mitofilin, VDAC1, VDAC2 and VDAC3 in SAM50 knockdown cells versus control HeLa cells. y axis: $2^{(-\Delta\Delta Ct)}$ value represents differences between the mean Ct (Cycle threshold) values of tested genes and those of reference gene (SDHA).

Figure S5

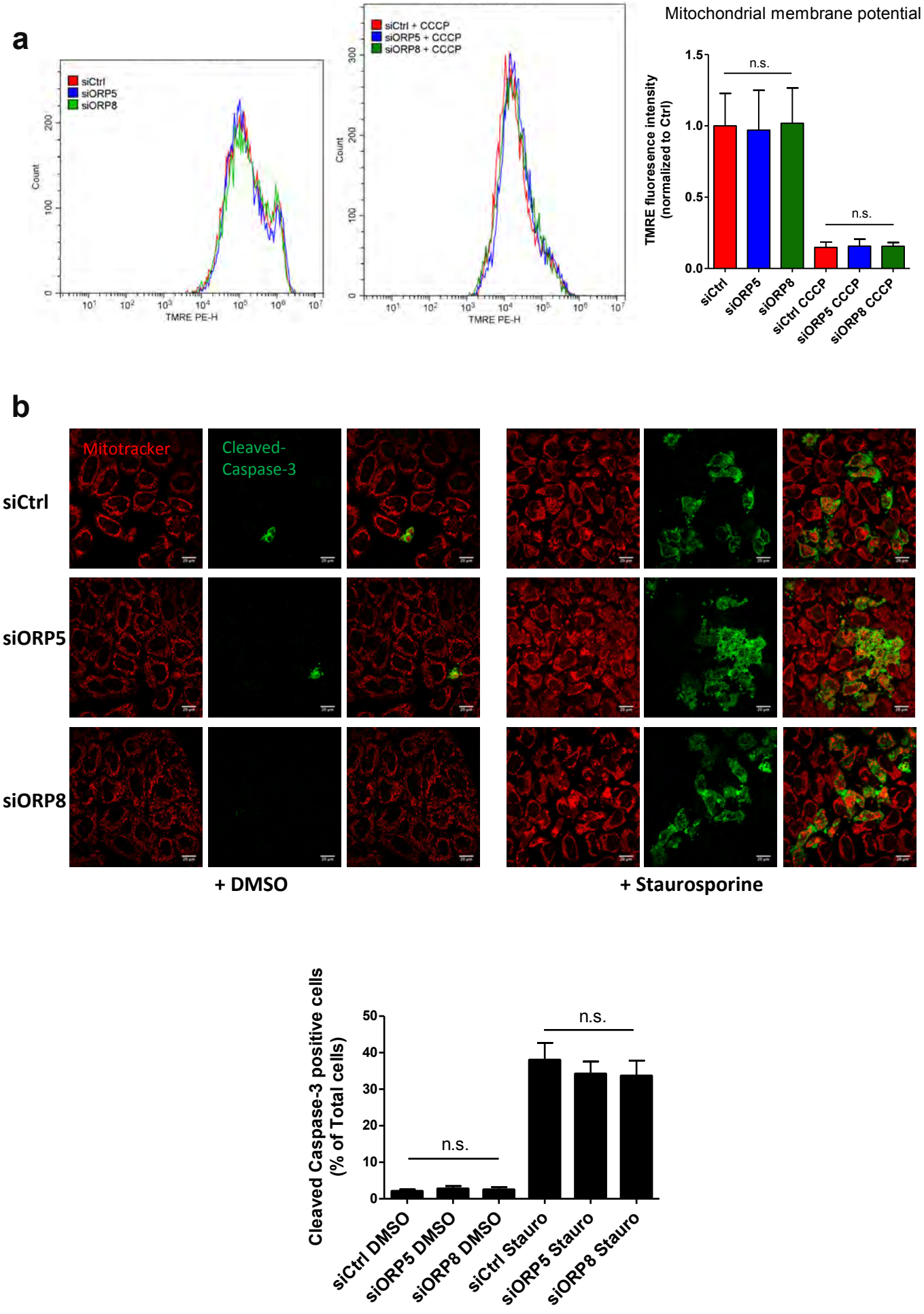
a
siCtrl
siORP5
siORP8
Count
TMRE PE-H
siCtrl + CCCP
siORP5 + CCCP
siORP8 + CCCP
Mitochondrial membrane potential
TMRE fluoresence intensity (normalized to Ctrl)
n.s.
n.s.
siCtrl
siORP5
siORP8
siCtrl CCCP
siORP5 CCCP
siORP8 CCCP
b
Mitotracker
Cleaved-Caspase-3
siCtrl
siORP5
siORP8
+ DMSO
+ Staurosporine
Cleaved Caspase-3 positive cells (% of Total cells)
n.s.
n.s.
siCtrl DMSO
siORP5 DMSO
siORP8 DMSO
siCtrl Stauro
siORP5 Stauro
siORP8 Stauro

Figure S6

Figure S6. (a) Representative graphs of flow cytometry analysis of HeLa cells transfected with siRNA against ORP5 or ORP8 (n = 10 000 cells) and loaded with the mitochondrial membrane potential sensitive dye TMRE, in presence (right graph) or absence (left graph) of CCCP. Flow cytometry histograms are showing the relative TMRE fluorescence intensity; the average of three independent replicates is shown. Data are presented as normalized mean ±SEM. (b) Fluorescent images of HeLa cells transfected with siRNA against ORP5, ORP8 or control, treated with DMSO or staurosporine and stained with anti-cleaved Caspase-3 (apoptotic cells) and Mitotracker. Scale bar, 20 μm. The graphs represent the means ±SEM of the percentage of cleaved Caspase-3 positive cells in the different conditions; the average of three independent replicates is shown, n.s; not significant.